

Review

State of the Art in Directed Energy Deposition: From Additive Manufacturing to Materials Design

Adrita Dass ¹ and Atieh Moridi ^{2,*}

¹ Materials Science and Engineering Department, Cornell University, Ithaca, NY 14850, USA

² Mechanical and Aerospace Engineering Department, Cornell University, Ithaca, NY 14850, USA

* Correspondence: moridi@cornell.edu

Received: 11 June 2019; Accepted: 24 June 2019; Published: 29 June 2019



Abstract: Additive manufacturing (AM) is a new paradigm for the design and production of high-performance components for aerospace, medical, energy, and automotive applications. This review will exclusively cover directed energy deposition (DED)-AM, with a focus on the deposition of powder-feed based metal and alloy systems. This paper provides a comprehensive review on the classification of DED systems, process variables, process physics, modelling efforts, common defects, mechanical properties of DED parts, and quality control methods. To provide a practical framework to print different materials using DED, a process map using the linear heat input and powder feed rate as variables is constructed. Based on the process map, three different areas that are not optimized for DED are identified. These areas correspond to the formation of a lack of fusion, keyholing, and mixed mode porosity in the printed parts. In the final part of the paper, emerging applications of DED from repairing damaged parts to bulk combinatorial alloys design are discussed. This paper concludes with recommendations for future research in order to transform the technology from “form” to “function,” which can provide significant potential benefits to different industries.

Keywords: additive manufacturing; directed energy deposition; process maps; laser engineered net shaping; dilution; solidification cooling rate; process-microstructure relationship

1. Introduction

Additive manufacturing (AM), also popularly known as 3D printing, is at the frontier of development for manufacturing diverse parts and has also been referred to as the third industrial revolution [1–3]. AM has an advantage over other conventional manufacturing techniques, making it possible to print complex shapes without the need for several conventional processing steps, such as expensive tooling, dies, or casting molds [3–5]. There are several reviews on AM covering different aspects from process dynamics to post-processing [6–10]. This paper focuses on one such type of AM process, popularly known as directed energy deposition (DED), (also more specifically as laser engineered net shaping (LENSTM), blown powder additive manufacturing, laser metal deposition system, and directed laser deposition), which has attracted significant attention due to its ability to print metals and potentially any metal-alloy system, notably functionally gradient materials [11,12]. Another important application utilizing DED is the remanufacturing or repairing of a component to increase its lifespan and hence reduce environmental impact [12,13].

DED systems have a concentrated energy source and a stream of raw material, both intersecting at a common focal point, generally in the presence of an inert shield gas. The energy density generated at a particular point melts the raw materials in and around that spot, giving rise to melt pool formation. There are various types of DED systems, which include (but are not limited to): Powder-feed and wire-feed based DED (on the basis of the type of feedstock), melt based DED, and kinetic energy based DED (on the basis of the type of energy source). Melt based DED could be further subclassified as laser

based DED, electron-beam based DED, plasma based DED, and electric arc based DED. The powder based DED system has been studied extensively in the literature and is the most commonly used metal DED technique. It predominantly uses a laser beam as the heat source. Wire based DED processes provide a lower resolution as compared to laser-beam powder based processes, but have a higher deposition rate and the ability to build larger structures [14,15]. They generally use an electron-beam, plasma, or electric arc as the heat source. Electron-beam based AM (EBAM), which has a high energy focused electron beam in vacuum, can fuse almost any metal. EBAM is commercialized by Sciaky, Inc. and it is mainly used for manufacturing near net shape parts [16]. Plasma based AM uses a controlled plasma source to melt the metal particles. This is a relatively new AM technology and is commercially being used by Norsk Titanium to build mainly titanium parts [17]. Electric arc based DED melts the wire feed to deposit the layers. Emerging technology, like metal big area additive manufacturing (mBAAM) [14], takes advantage of the principle of electric arc welding to print big parts. Kinetic energy based DED systems, often referred to as Cold Spray, use a converging-diverging nozzle to accelerate micron sized particles to supersonic velocities [18]. Beyond a critical impact velocity, micron sized particles adhesively bond to the substrate and build up material in the form of a coating as well free standing bulk components [19]. Figure 1 summarizes the different DED categories in the form of a flowchart.

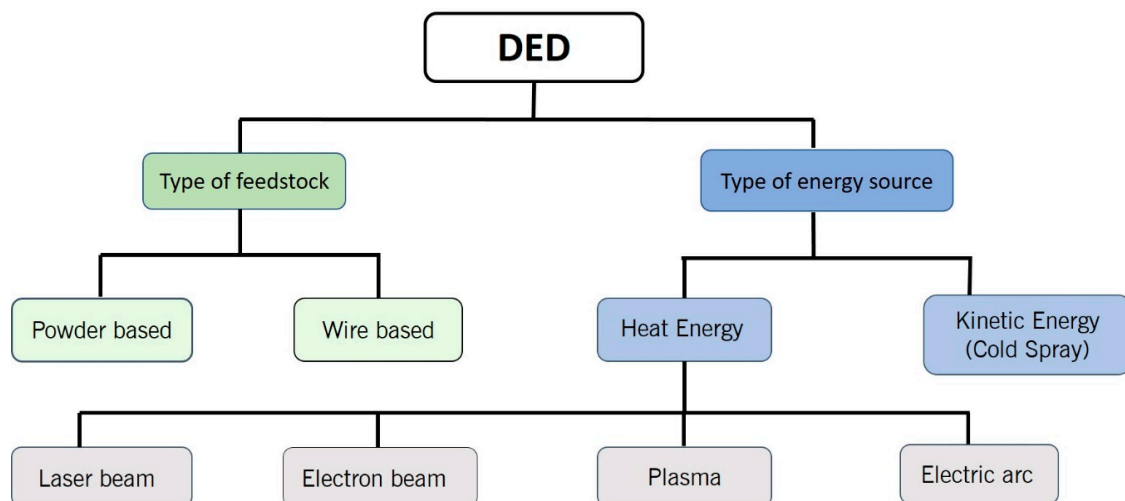


Figure 1. Classification of Directed Energy Deposition (DED) systems.

This paper will focus on the powder based DED systems in detail. It covers sections on metal and alloy systems, emphasizing the potential of DED, modelling efforts and process variables (surface tension, Marangoni effect, dimensionless numbers, energy distribution in a DED process, process-microstructure relationships, dilution), common defects (porosity, solute segregation and changes in chemical compositions, printability of alloys), mechanical properties (tensile strength, hardness, fatigue, residual stress), DED process control and monitoring, determination of optimal processing parameters by establishing process maps and the regions where high amount of defects are expected, application, and emerging technologies (DED of metal parts in biomedical applications, welding and cladding, repair, bulk combinatorial alloy design, construction materials, and hybrid AM). The paper will conclude with an overview of possible future perspectives of the field.

Metal and Alloy Systems

DED has been used to print mainly functionally graded materials, metal-matrix composites, and coatings. Each system was developed for a targeted application (e.g., enhancing biocompatibility, improving oxidation resistance, mechanical, and tribological properties, interfacial strength, etc.). Table 1 summarizes selected material systems with an emphasis on the potential applications.

Table 1. Selected studies showing DED as an emerging method to print complex metal and alloy systems.

Material System	Reported Functionality or Application or Process Optimization as Applicable *	References
Ni coated TiC on Inconel 625	Improved mechanical properties	[20]
Invar + TiC	Invar has a very low coefficient of thermal expansion which was used to make parts with low thermal stresses	[21]
Ti-48Al-2Cr-2Nb + TiC	Used to study optimum process parameters, high temperature structural applications and it exhibited twice the hardness of Ti-6Al-4V	[22]
TiC/Ti	Combines the high temperature and wear resistance of ceramics with good mechanical properties of metals	[23]
VC on SS304	Ultrahigh temperature coating on stainless steel to improve high temperature performance	[24]
Ti-6Al-4V-Al ₂ O ₃	Conventionally processed ceramics requires post-processing (e.g., high temperature sintering), but this compositionally graded ceramic deposit on Ti-6Al-4V (having compositions, like pure Ti-6Al-4V, Ti-6Al-4V + Al ₂ O ₃ , and pure Al ₂ O ₃) can be achieved in one step using computer aided manufacturing, thereby reducing the need for post-processing	[25]
Ti-TiO ₂	TiO ₂ on the surface of porous Ti increases surface wettability and biocompatibility	[26]
Compositionally graded alumina on SS303	Better interfacial properties of coating due to growth of Al ₂ O ₃ coarse columnar microstructure in the direction of deposition	[27]
CoCrMo on porous Ti-6Al-4V	Porous implant that can eliminate stress shielding issue associated with fully dense implants and CoCrMo coating can improve the biocompatibility	[28]
Ti + SiC	Good electrochemical and tribological properties, non-toxic for biological implants	[29,30]
Calcium phosphate on Ti	Load bearing implants with high hardness and wear resistance	[31]
CNT (carbon nanotubes) + calcium phosphate + Ti-6Al-4V	Tribo-film formation improved wear resistance for Ti-6Al-4V, CNT facilitated in-situ carbide formation enhancing hardness	[32]
Ti-Zr-BN	Demonstrated superior mechanical properties with respect to pure Ti; could be used to improve surface and bulk properties.	[33]
Hydroxyapatite (HA) coating on Ti-6Al-4V	Deposition of Ti/HA interfacial layer on Ti-6Al-4V using LENS™, followed by plasma spraying of HA, to improve bond strength and increase osteoconductivity of metallic implants	[34]
Ni-18Al-11Cr-9C and Ni-14Al-8Cr-29C	Improved wear resistance	[35]
YSZ (yttria stabilized zirconia) on Ni based superalloy	Good thermal barrier protection and good thermal cycling resistance	[36]
ZTA (zirconia toughened alumina)	ZTA is tougher than pure alumina, making it useful in many industries, but it exhibits poor surface quality and therefore was post-processed using rotary ultrasonic machining, which combines both grinding and ultrasonic machining processes	[37]

Table 1. Cont.

Material System	Reported Functionality or Application or Process Optimization as Applicable *	References
Inconel and ceramic powders	Optimized the process parameters with the help of mode FRONTIER [®] software that helped minimize energy consumption and material wastes, and maximizes powder melting	[38]
Ti-Si-N coatings on Ti	Higher hardness and wear resistant coatings on Ti (with varying ratios of Ti-Si, higher Ti content lead to higher hardness)	[39]
Lead zirconate titanate (PZT)	Reasonable dielectric properties achieved with DED without post-processing, can be used potentially in the PZT embedded sensors and transducers on structural materials	[40]
Alumina (Al ₂ O ₃)	Easier manufacturing of refractory materials by DED compared to expensive and difficult traditional processing techniques	[41–45]
Al ₂ O ₃ + YAG (yttrium aluminum garnet)	This eutectic ceramic with water-cooled substrate showed a 10% increase in microhardness and a fracture toughness increase of 8.5%, compared to non-water cooled substrate	[46]
Tri calcium phosphate (TCP) ceramic	Good biocompatibility with cell differentiation ability for load bearing bone implants	[47]
Al ₂ O ₃ + ZrO ₂	DED with ultrasonic vibrations helped in achieving crack free parts and good mechanical properties	[48,49]
Al ₂ O ₃ -ZrO ₂ (Y ₂ O ₃) eutectic ceramic structures	Direct fabrication by DED without binders, having acceptable mechanical performance	[50]
Ni-Ti	Influence of laser power on the properties of DED fabricated equi-atomic Ni-Ti composition and the effect of laser power on corrosion resistance	[51]
SS316L	Greater resistance to corrosion after heat treatment	[52]
Nb-Ti-Si-Cr	High temperature structural strength and oxidation resistance	[53]
Fe-Cr-Ni-Mo-W-B	Optimized volume of hard precipitates using CALPHAD, achieved crack free deposition on carbon steel substrate when it was preheated to 400 °C	[54]

* This table shows potential for printing diverse combinations of materials with DED, rather than looking at all applications or functionalities in great detail.

2. DED Process Variables and Modelling Efforts

2.1. Overview of Powder-Fed DED Process Physics and Thermal History

DED is a non-equilibrium processing technique, which has very fast cooling rates, often on the order of 10³ to 10⁵ K/s [55,56] for laser and electron beam energy sources. Major process parameters for laser based DED include: Laser power, laser beam spot size, powder or wire feed rate, scanning speed, carrier gas flow rate, clad angle, feedstock properties, and layer dimensions. Therefore, a diverse set of processing parameters coupled with the complex transport phenomena, including conduction of heat into the substrate, convection due to Marangoni effects, and radiation accompanied by the shield gas, lead to a difficulty in understanding the effect of these individual process parameters on the overall DED process. Figure 2 schematically shows the complex thermal history during the multi-layer DED process, and the trend of an increasing peak temperature with an increasing layer number due to the accumulation of heat in the system [57].

Modelling efforts are beneficial to complement experimental data. The model should be close to the real DED system, taking into account the transient temperature and heat flow, complex transport

phenomena, heating and cooling cycles, solidification rate, etc. These in turn give important information about the microstructure, defects, texture, and mechanical properties [57]. Table 2 summarizes some important modelling efforts of the DED process in the literature.

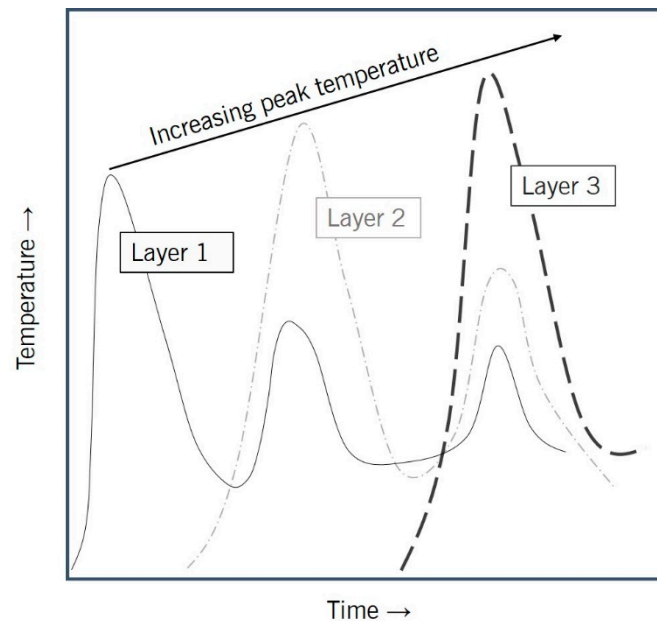


Figure 2. Schematic showing the thermal cycles for three consecutive layers during DED, and the corresponding peak temperatures for each layer.

Table 2. Selected studies on the modelling efforts of various DED processes.

Model	Explanation	Reference
Powder stream mass and temperature of the melt pool	Mass flow model taking into account powder flow into the melt pool using negative enthalpy method (subtracting the mass out of the model compared to the one considering no mass).	[58]
Powder flow trajectory simulations	The powder catchment efficiency was dependent on the carrier gas flow rate, with a higher flow rate giving more catchment; bigger powders had a smaller velocity due to inertia, leading to less catchment efficiency. Smaller powders also had less catchment efficiency.	[59]
Forced convection events	This model takes into account forced convection effects due to inert gas flow inside the chamber, and also the powder flow along with the inert gas, to reduce errors in simulations.	[60]
Powder nozzle physics	Numerical simulations to study the powder flow and determine the contribution of nozzle geometry in affecting the powder flow.	[61]
Columnar to equiaxed transition	Thermal modelling and computational thermodynamics to study microstructure heterogeneity during AM.	[62]
Phase transformations in Ti-6Al-4V	Large scale phase field modelling approach to predict the localized phase transformations in Ti-6Al-4V.	[63]
Heat transfer and cooling rates during DED	Modelling of melt pool temperatures, velocities, cyclic thermal cooling behavior, and peak temperatures.	[64–68]
Residual stress evolution	Simulations of localized residual stresses using finite element analysis, and assuming quasi-static models.	[69,70]

2.2. Surface Tension and Marangoni Effect

The Marangoni effect is a convective heat transfer phenomenon, which affects the melt pool flow dynamics and indirectly contributes towards porosity, which is a major concern in DED processed materials. In 1982, Heiple and Roper [71] postulated the theory that Marangoni forces generated due to the differences in surface tension and temperatures along the melt pool lead to more spattering and circulation of the liquid melt pool. The movement is mainly from regions of high surface tension to low surface tension (γ), finally leading to variable melt pool penetration. The strength of the Marangoni flow for any DED process can be determined through the dimensionless Marangoni number (M_a) [72], as provided in Equation (1):

$$M_a = \frac{d\gamma}{dT} \frac{dT}{dx} \frac{L^2}{\eta\alpha} \quad (1)$$

where γ is the surface tension, dT/dx is the temperature gradient, α is the thermal diffusivity, L is the characteristic length, and η is the viscosity of the melt pool. The surface tension gradient (the slope of the graph) qualitatively governs the melt pool movement. Figure 3 schematically shows how the variation of the surface tension with temperature affects the melt pool geometry. Figure 3a shows how the melt pool length is small due to a negative surface tension gradient and signifies bulk turbulence flow in the melt pool. Figure 3b shows how the melt pool depth increases with a positive gradient of surface tension and surface turbulence occurs in the melt pool, which could also potentially trap undesired oxides in the bulk. Figure 3c shows the transition from a positive to negative surface tension gradient at a certain temperature, T_o . This transition also indicates a melt pool flow transition from surface turbulence to bulk turbulence. The surface tension and therefore the internal melt pool flow could be controlled, to a certain extent, using surface active elements. For example, in an Fe system, changes in the concentration of the surface-active elements, like sulphur and oxygen, were shown to modify the internal melt pool flow [72,73].

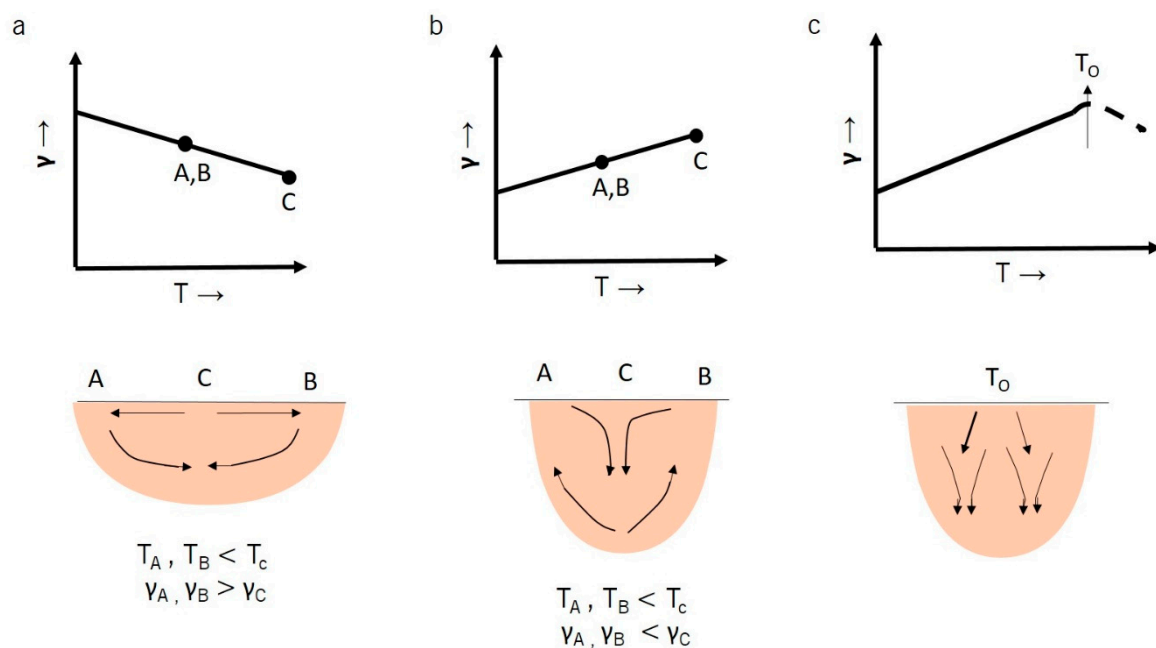


Figure 3. Schematic of Marangoni effect using the Heiple–Roper theory of weld pool geometry, depending on the surface tension and temperature of the melt pool, as applicable for DED systems. (a) Melt pool geometry when the surface tension gradient is negative, (b) melt pool geometry when the surface tension gradient is positive, and (c) melt pool geometry when the surface tension gradient shifts from positive to negative.

Besides the Marangoni flow force, other forces, like aerodynamic drag (outward drag forces caused by the plume formed above the melt pool), buoyancy (upward movements of the melt pool due to density changes caused by thermal gradients inside the melt pool), electromagnetic, and Lorentz forces (forces due to electric and magnetic fields generated by the source), may also be present during the DED process [72].

2.3. Dimensionless Numbers

Other than the Marangoni number, there are several other dimensionless numbers which enable capturing of the accumulative effect of various process parameters [74]. While these dimensionless numbers are not specifically developed for DED, they can capture the DED process variable relationships very well. Table 3 summarizes three such dimensionless numbers for laser based DED systems (these can be extended to other heat sources as well).

Table 3. Dimensionless numbers and their definitions.

Name	Formula *	Definition	Literature Reported
Non-dimensional Heat Input	$Q^* = \frac{P/V}{P_r/V_r}$ where P is the laser power, V is the scanning speed, P_r is the reference laser power, and V_r is the reference scanning speed (P_r and V_r provide the lowest heat input per unit length of deposited material)	Energy per unit length of material used to deposit layers	[74]
Peclet Number	$Pe = \frac{UL}{\alpha}$ where U is the characteristic velocity, α is the thermal diffusivity of the alloy, and L is the characteristic length.	The relative strength of convection to conduction in the system	[75]
Fourier Number	$F_0 = \frac{\alpha}{L^2}$ where α is the thermal diffusivity, τ is the characteristic time scale, and L is the characteristic length	Gives relative value between heat dissipation and heat storage rates	[76]

* Characteristic length refers to either the thickness of the layers, the melt pool width or depth, and the laser beam spot size; characteristic velocity is considered to be the maximum velocity of the molten metal; characteristic time is defined as the length of the melt pool divided by the scanning speed.

2.4. Energy Distribution in a DED System

During DED, there should be conservation of mass, momentum, and energy, like any other physical system. Therefore, keeping track of how the initial heat source energy is distributed during the process will be beneficial in further improving the DED process to reduce energy loss and maximize energy for melting powders. Calorimetric measurements of the energy absorbed by the substrate (Q_{ABS}), energy absorbed by the powder (Q_{DEP}), energy reflected by the substrate (Q_{REF}), and energy lost by the powder (Q_{LOST}) due to evaporation and lack of fusion for DED of Ti-6Al-4V and Inconel were performed in the literature [77]. The important parameter is the bulk absorption coefficient (β), which gives the ratio of the energy for a particular component of energy (Q_{ABS} , Q_{DEP} , Q_{REF} , or Q_{LOST}) with respect to the total energy supplied to the system (Q_{IN}). The energy balance equation is shown in Equation (2) and the corresponding bulk absorption coefficient, β , is presented in Equation (3) [77]:

$$Q_{IN} = Q_{ABS} + Q_{DEP} + Q_{REF} + Q_{LOST} \quad (2)$$

$$\beta_{ABS} + \beta_{DEP} + \beta_{REF} + \beta_{LOST} = 1 \quad (3)$$

where β_{ABS} refers to the bulk absorption coefficient due to Q_{ABS} , β_{DEP} refers to the bulk absorption coefficient due to Q_{DEP} , β_{REF} refers to the bulk absorption coefficient due to Q_{REF} , and β_{LOST} refers to the bulk absorption coefficient due to Q_{LOST} . From this study, it was experimentally proven that about

60% of the total initial energy was lost when using a laser as heat source, due to reflection by powders and also by powders not absorbing enough energy to melt.

2.5. Process–Microstructure Relationship

The energy source used during DED can be approximated as the Rosenthal solution of a moving heat source (laser, electron beam, plasma, or arc) on an infinite substrate. The microstructures obtained through DED can be predicted using the two important parameters: Thermal gradient, G (K/cm), and solidification front velocity (or interfacial velocity), R (cm/s). The relationship between G and R gives the thermal process maps [78,79]. Figure 4 shows graphs describing relationships between parameters, like G , R , arc length, undercooling, and supercooling. The mathematical relationships for the cooling rate, thermal gradient, and solidification front velocity are as follows (the reader could refer to [56] for a derivation of these equations):

$$\text{Cooling rate : } \frac{\partial T}{\partial t} \tag{4}$$

$$\text{Thermal Gradient : } G = |\nabla T| \tag{5}$$

$$\text{Solidification front velocity : } R = \frac{1}{G} \frac{\partial T}{\partial t} \tag{6}$$

where T is the temperature and t is the time. The melt pool circumference (MPC) length used in Figure 4 is the length of the circumference of the melt pool, and measurement starts from the bottom to the top of the melt pool in this study.

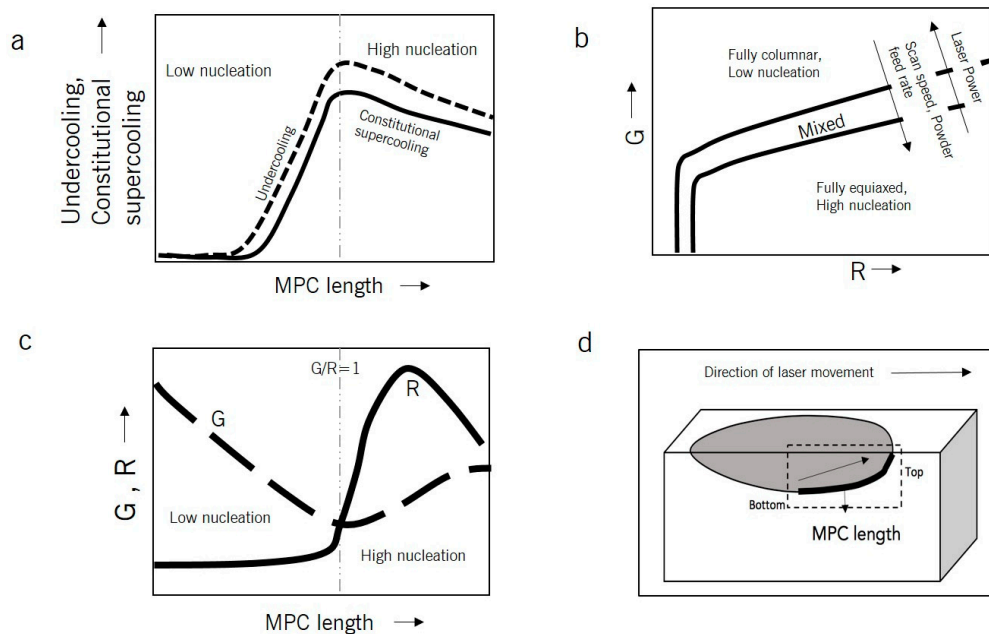


Figure 4. The relationships explaining the process maps for G vs. R , derived from [80]; (a) graph of undercooling/constitutional supercooling versus melt pool circumference (MPC) length showing the transition from low nucleation to high nucleation (columnar to equiaxed transition), (b) trend of the columnar to equiaxed transition from the graph of G versus R , (c) variation of the G/R ratio with respect to the MPC length, and (d) the MPC length as defined from the bottom to the top.

Some of the important trends derived from solidification front velocity and thermal gradient studies are:

- Cooling rates as high as 13,000 K/s were recorded in the literature during in-situ process monitoring of Ti-6Al-4V with laser based DED [81]. The initial cooling rates and microstructures changed with an increase in the number of deposited layers. This may be due to the accumulation of thermal energy in the part as more layers are deposited. This is proven in a study of Ti-6Al-4V printed with laser based DED, wherein a martensite microstructure formed in the first layers slowly convert to a Widmanstatten microstructure as the layers build up [82].
- According to the literature, the microstructure of laser based DED processed Ti-6Al-4V was columnar near the substrate (smaller MPC length) and equiaxed away from the substrate (higher MPC length) (due to differences in cooling rates), and there was a superheated melt pool during the process (almost 40%–50%) [81]. Figure 4a shows the relationship between undercooling and constitutional supercooling with respect to the MPC length.
- Heterogeneous nucleation varies with respect to the scanning speed, powder feed rate, and heat source power as shown in Figure 4b. Increases in the scanning speed and powder feed rate or decreasing the heat source power decreases the thermal gradient, G . That leads to an increase in R and a higher amount of equiaxed structure in the part.
- The ratio of G/R is an important parameter. $G/R > 1$ means a low rate of nucleation, due to a thermal gradient that is greater than the solidification front velocity, and $G/R < 1$ means a high rate of nucleation, due to a thermal gradient that is smaller than the solidification front velocity, as shown in Figure 4c.
- Figure 4d shows the MPC length, and increases in the value from the bottom to the top of the melt pool.

To conclude, as the MPC length increases, there is an increasing trend of undercooling and constitutional supercooling, leading to more columnar-to-equiaxed transition (CET), till the G/R ratio reaches 1. Therefore, CET is dictated by the thermal history and can be engineered according to requirements [80].

2.6. Dilution

DED involves the printing of subsequent layers of material to build a final part. There is heat accumulation due to multi-track and multi-layer deposition, and that will change the microstructure and final properties of the printed parts. A minimum level of metallurgical bonding is required between subsequent layers, which can be quantified using a dimensionless parameter called dilution. Dilution can be defined as:

$$D = \frac{d}{h + d} \quad (7)$$

where d is the depth of the melt pool below the substrate level, and h is the height of the material deposited above the substrate level. A high value of h correlates to a higher powder flow rate or lower energy input (corresponding to low dilution and lack of fusion between different layers), whereas a high value of d is due to a lower powder feed rate or higher energy input (corresponding to high dilution and keyholing phenomenon). There is an optimum value for dilution, which results in a good metallurgical bonding [83]. Figure 5b shows the optimal dilution level in a metal-substrate system generally between 10% and 30%, which is the standard value adopted by several researchers [84], and Figure 5a,c shows the extreme cases of dilution (<10% and >30%, respectively).

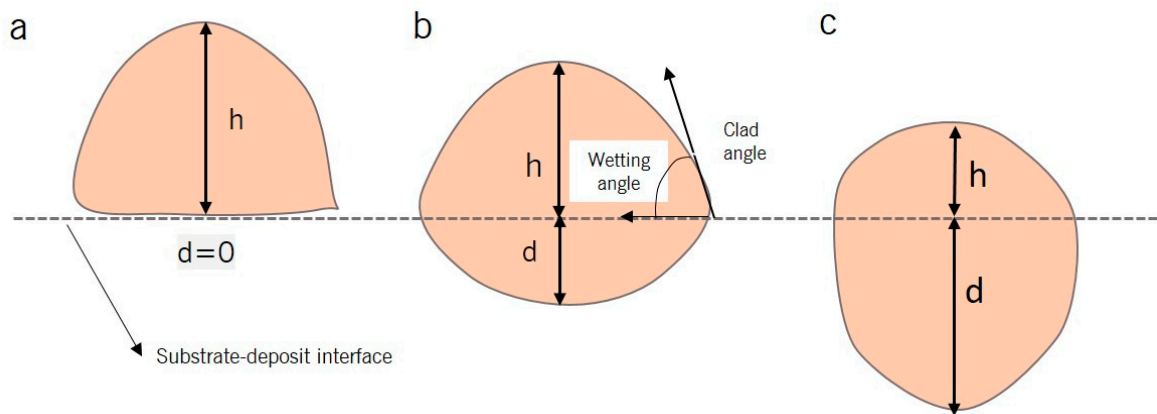


Figure 5. (a) Zero penetration ($d = 0$) or low penetration, meaning a lack of fusion with the substrate; (b) optimal level of dilution (generally between 10% and 30%); (c) high d leads to keyholing.

3. Common Defects

Defects may arise in the material during manufacturing. It is important to know the cause of such defects and take effective measures to counteract them. The most common defects arising during DED are discussed in the following sections.

3.1. Porosity

Porosity is one of the most important defects, which is linked to mechanical properties of DED processed parts. There are two major types of porosities: Interlayer porosity and intralayer porosity. Interlayer porosity occurs due to a lack of sufficient energy input to melt the filler material (powder or wire), leading to un-melted regions. This happens near the substrate or between un-melted tracks, when the linear heat input (heat source energy/scanning speed) is decreased or the mass flow rate is increased or a combination of the two. Interlayer pores are usually large and irregular in shape and occur due to higher solidification cooling rates. Low dilution values also cause the occurrence of interlayer porosities. Intralayer porosity is linked to the use of inert shielding gas during the DED process, promoting gas entrapment. Intralayer pores are usually spherical in shape and occur at random locations, owing to vaporization leading to gas trapped porosities, and observed within regions having lower solidification cooling rates [82,85,86]. High dilution refers to the occurrence of intralayer porosities. Interlayer and intralayer porosities are schematically shown in Figure 6a,b, respectively. Porosity is also dependent on the initial powder characteristics and uniformity [87]. If the starting powders do not have a uniform size distribution, it will give rise to more porosity in the final build. Inherent porosity inside the powder particle also leads to defects in the final part [88]. Taking all these modes of porosities into account, it is important to control the shape and size range of powders, and also maintain optimal process parameters during deposition. Porosity can be measured both qualitatively and quantitatively. Some commonly used techniques include the Archimedes principle, X-ray computed tomography, and optical microscopy.

Another important parameter in the literature, referred to as the global energy density (GED), establishes a relationship between interlayer (lack of fusion) and intralayer (keyholing) porosity:

$$\text{GED} = \frac{P}{vd} \quad (8)$$

In Equation (8), GED is defined for laser based DED, where P is the laser power, v is the scan speed, and d is the laser spot size. GED can be easily correlated with dilution. As shown in Figure 6c, lower values of GED lead to less dilution (the negative slope), meaning more propensity to a lack of fusion defect, whereas higher values of GED lead to high dilution (the positive slope), meaning more tendency to form keyhole porosity [85].

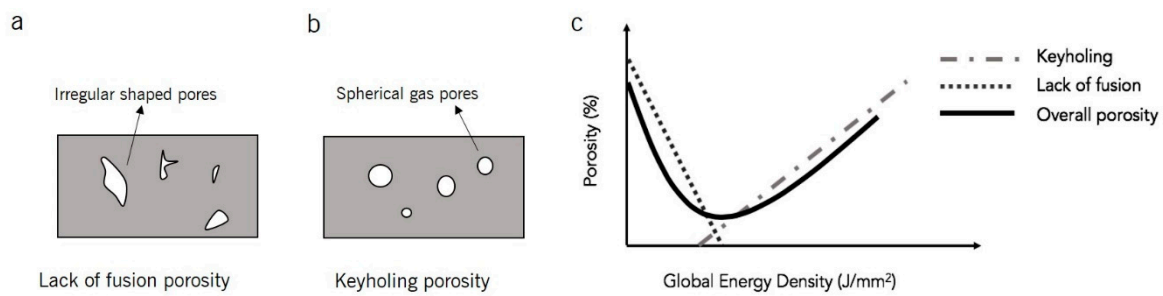


Figure 6. Schematic of: (a) Lack of fusion porosity (interlayer porosity), (b) keyholing porosity (intralayer porosity), and (c) the intersection of interlayer and intralayer porosity with respect to global energy density (GED).

3.2. Changes in Chemical Compositions due to Solute Segregation and Loss of Alloying Elements

When several layers are deposited during AM, it gives rise to the redistribution of solute particles, leading to the segregation and formation of heterogeneous microstructural bands, also known as heat affected zone (HAZ). This happens due to differences in the compositions at the interfaces of the substrate and deposit. The amount of solute segregation also depends upon the solidification cooling rates, with higher solidification cooling rates having a higher probability of a solute trap. These changes give rise to compositional inhomogeneity along the printed material [89,90]. Another phenomenon, the loss of alloying elements, occurs due to the preferential vaporization of a few elements in the alloy during DED, due to differences in the boiling points of individual elements. For example, in a study of printed 304L stainless steels, compositional gradients developed along the build direction due to a greater loss of volatile elements (e.g., Cr, Mn, and Ni) as more heat built up in the system. The loss of these austenite stabilizers led to an increased hardness in the build direction due to the presence of a more martensitic phase in the upper layers [91]. The Langmuir equation can quantitatively predict the vaporization flux of the alloying elements, given by [65]:

$$J_i = \frac{\lambda P_i}{\sqrt{2\pi M_i T}} \quad (9)$$

where J_i is the vaporization flux of alloying elements, M_i is the molecular weight, P_i is the vapor pressure of the alloying elements, T is the temperature, and λ is a positive fraction, which estimates the condensation of some vaporized atoms. Consecutively, the mass of material vaporized can be estimated by:

$$\Delta m_i = \frac{L A_s J_i}{v} \quad (10)$$

where Δm_i is the mass vaporized, L is the track length, A_s is the melt pool area, v is the scan speed, and J_i is the vaporization flux of alloying elements. An example where the above equations were applied to estimate the amount of material lost during AM inferred that Al in Ti-6Al-4V is most susceptible to composition changes during DED, followed by Mn in stainless steel 316, with the least susceptible being Cr in Inconel 625 [92].

3.3. Printability of Alloys

Not all alloys are suitable to be processed by AM. Quantitatively, the printability of alloys could be defined using a dimensionless parameter known as thermal strain (Equation (11)). Lower values of thermal strain cause lesser residual stress in the material, thereby increasing the printability of the alloy by AM:

$$\epsilon^* = \frac{\beta \Delta T}{EI} \frac{t}{F \sqrt{\rho}} H \quad (11)$$

where β is the bulk thermal expansion coefficient, ΔT is the change in temperature, t is the deposition time, H is the heat input, EI is the flexural rigidity, F is the Fourier number, and ρ is the density of material (the derivation of this particular equation has been performed in literature [92]). So, with an increase in $\beta\Delta T$, t , and H , there is an increase in the thermal strain, whereas an increase in EI and F can decrease thermal strain.

4. Mechanical Properties

4.1. Tensile Strength

The tensile strength and ductility of printed parts is dependent on the DED process parameters and the microstructure. There are several instances from the literature, which record varying trends of tensile behavior and ductility for the same material printed by DED. For instance, in one study, the tensile strength of DED fabricated Ti-6Al-4V was found to be similar to wrought manufactured Ti-6Al-4V, but with reduced ductility [93]. Another study showed that DED processed Ti-6Al-4V has a higher tensile strength due to a finer microstructure as compared with wrought alloy, but still exhibits lower ductility, due to a combination of the fine microstructure and the presence of internal defects [94]. Yet another study on DED processed parts showed an anisotropic porosity and tensile behavior in three different orientations, due to microstructural anisotropy [95]. The same study also demonstrated that with a 0.0124% increase in oxygen and decrease in the alpha lath width of DED processed Ti-6Al-4V, the yield strength and ultimate tensile strength (UTS) increased without any change in ductility. Post-processing, like heat treatments or hot isostatic pressing, tends to improve the ductility with a slight decrease in the tensile strength [94].

4.2. Hardness

Microhardness values can change along the build direction due to variations in the microstructure. The microhardness is higher near the first and the last layers, and relatively lower in the central layers. This variation could be attributed to the cyclic thermal history during the DED process. There is a higher heat buildup in the central layers, resulting in lower microhardness values [96]. A higher hardness and finer microstructure was reported in the literature by increasing the substrate thickness (more substrate mass acts as a faster heat sink). Increasing the substrate temperature decreased the hardness, due to a decrease in the thermal gradients and cooling rates, which can lead to a coarser microstructure. A higher interlayer dwell time is also known to increase the hardness, due to steeper thermal gradients [82]. Hardness studies by Zuback et al. stated that post processing of AM parts (like heat treatment or aging) or alloy selection could give more control over hardness, rather than changing the DED process parameters [97].

4.3. Fatigue

Fatigue is an important criterion for determining the structural integrity of materials printed by DED. The fatigue properties of AM parts have been studied by several groups [98–100] and recently reviewed by Bian et al. [101]. Fatigue is influenced significantly by the microstructure and defects [102]. In DED processed parts, the fatigue life can be estimated by determining the fatigue crack growth and number of probable fatigue initiation sites (or pores) [9]. Another fatigue initiator is un-melted powders, which could subsequently reduce the fatigue life by an order of magnitude [103]. In-situ high energy X-ray microtomography tests for fatigue crack propagation data at Argonne Photon Source (APS) were correlated with fatigue data from other conventional fatigue testing techniques (i.e., direct current potential drop techniques and fracture surface striations) [93]. It was found that fatigue crack growth was mostly in plane, with some cracks propagating towards the direction of tensile force. The crack growth rate was found to vary along different directions, and was also location dependent [93]. As of now, there is still a lack of consistency in the fatigue behavior reported by several authors. For instance, a study of LENSTM processed Ti-6Al-4V found a better high cycle fatigue

life with respect to cast Ti-6Al-4V [104], while another study found a similar high cycle fatigue life for both LENSTM and wrought materials [103]. Another study stated that as-deposited DED shows similar properties to those of cast Ti-6Al-4V, while heat-treated DED Ti-6Al-4V has similar properties to those of wrought Ti-6Al-4V [94]. Hot isostatic pressing (HIP) improved the fatigue life of DED parts, by closing the porosities inside the parts [105]. As fatigue data is crucial to understanding the damage tolerance of structural materials, a lot more research is required in this field to establish accurate predictions of fatigue properties.

4.4. Residual Stress

Residual stress (RS) is generated during DED or any other metal AM technique due to the presence of steep thermal gradients between the heat source and the surrounding material. RS has the ability to damage the printed parts, due to distortion and cracking. RS is different at different locations in the printed metal. Studies have shown that residual stresses near the surface are tensile in nature, while the ones in the center are compressive stresses. RS tends to be higher when they occur between dissimilar materials [56]. Maximum RS was observed at the substrate–deposit interface. RS in metal AM can be broadly classified into two types based on the length scale: On the macroscale and on the microscale and nanoscale [106]. RS measurements on the macroscale are most widely used and can be conducted using non-destructive techniques, like X-ray diffraction and neutron diffraction [89]. Different methods can be used to relieve or reduce residual stresses. The most common techniques are: Preheating the substrate or preheating the initial feedstock to decrease the steep thermal gradients; using in situ process monitoring with feedback control to tune the process parameters on the fly; or using ex-situ post processing techniques, like heat treatment, to relief RS [106].

5. DED Process Control and Monitoring

Controlling the DED process is complicated due to the potential involvement of more than one type of material and also due to high build volumes, making it prone to defects. Also, the majority of users rely on expensive and time-consuming techniques, such as multiple experimental runs, to define optimized process parameters. The National Institute of Standards and Technology (NIST) highlights this issue and acts as a catalyst to resolve the issue of non-uniformity in printed parts by developing better process monitoring protocols for faster industrialization of DED [107]. For example, porosity control in a DED system is crucial, as it directly affects the structural integrity of the part. Some efforts made towards DED process control are tabulated in Table 4. However, these studies do not provide comprehensive information on how the material's thermo-mechanical properties change dynamically during the process. Hence, there is a need for the application of robust scientific techniques which could counter these limitations and help us monitor material related properties dynamically. Recent developments in quality monitoring includes high-energy X-ray synchrotron studies of DED. These encompass: High energy synchrotron X-ray source and high speed imaging camera used in tandem to detect the in situ melt pool geometries and deduce the phase transformations of Ti-6Al-4V [108]; a piezo driven powder delivery in conjunction with a laser heat source to investigate the powder–melt pool interaction during printing of Ti-6Al-4V [109]. These studies provide insights into the DED process physics, but are still far from mimicking all the components in a real DED system. Hence, there is still lack of data for real industrial DED systems and future research in this area is required.

Table 4. Selected studies on DED process monitoring.

Study Technique	Function	Reported Literature
In-situ acoustic monitoring	Detects defects and cracks during process	[110,111]
Non-destructive thermographic inspections like IR cameras	Captures the thermal history	[81,112]
IR two wave pyrometers and high-speed CCD cameras	Monitors the melt-pool characteristics and temperature	[81,113–118]
High energy X-ray diffraction and imaging	Detects phase transformations and melt pool dynamics	[73,108,109]
Repetitive process controller	Used to optimize layer height during the process	[119]

6. Determination of Optimal Process Parameters for Laser Based Powder-Fed DED

DED is an emerging field in the area of metal AM, and our goal was to create efficient process maps which provide a holistic picture of the DED process parameters. This is expected to save the user time, money, and effort to design their experiments. Inspiration was taken from the work of M. Thomas et al., who created normalized process diagrams for selective laser melting using dimensionless numbers [120]. However, DED has an additional parameter of the powder feed rate. After scrutiny, the linear heat input and powder feed rate were selected as primary parameters to make the process maps. The corresponding equations for these parameters are as follows:

$$\text{Linear heat input} = \frac{P}{v} \quad (12)$$

where P is the laser power, v is the scanning speed of the laser, and:

$$\text{Powder feed rate} = \frac{M}{t} \quad (13)$$

where M is the total mass of the powder and t is the time to deposit powders. The linear heat input is a standard parameter which has been used often in the literature, normalized using the ratio of the two fundamental parameters: Laser power and scanning speed [74]. The linear heat input can be used for any range of values for the power and scanning speed, and it has been proven experimentally that the same linear power density gives similar properties [121]. Some previous studies have attempted to build DED process maps, based on the linear mass density [122,123], where:

$$\text{Linear Mass Density} = \frac{\frac{M}{t}}{v} \quad (14)$$

However, the linear mass density is not a robust parameter, as it fails to consider the influence of the effective residence time of the laser beam spot per unit volume of the powder feed. A higher scan speed or a higher powder feed rate will result in a lower effective residence time of the laser spot per unit volume of powder. To understand the consequences due to a less effective residence time, consider two extreme cases of process parameters, one having a high speed and high mass flow rate, and the other having a low speed and low mass flow rate. Even though both cases produce the same value of linear mass density, their properties are significantly different [122]. The high speed and high mass flow rate case will have worse properties due to the much lower effective residence time. To counteract such problems associated with the linear mass density and to be consistent irrespective of the varying range of values, the linear heat input was chosen to construct process maps.

The other unique DED parameter is the powder feed rate, which is not applicable for other AM systems, like powder bed fusion, selective laser melting, etc. Powder feed rate values will determine how much powder is transferred to the laser spot area. The powder catchment efficiency

varies, depending upon process parameters, like the feed rate, carrier gas flow rate, particle size, and velocity, etc., and it determines the percentage of the total powders that gets inside the melt-pool [59]. A material utilization efficiency of about 70% to 90% was reported for DED of Ti-6Al-4V powders [124]. Insufficient heat input or a very high powder feed rate also leads to unmelted powders.

A graph of the linear heat input versus the powder feed rate is plotted using selected data points from the literature, as listed in Table 5. The criterion for the selection of these specific data points was on the basis of their corresponding values of dilution. As mentioned in Section 2.5, about a 10% to 30% dilution represents a good amount of metallurgical bonding between subsequent layers (the clad dimensions are related to the scanning speed and powder feed rate of the DED process. These consecutively affect the contact angle, which determines the bonding of the deposit to the substrate, and overall, these quantities can be understood through the dilution parameter). However, there might be exceptions to the optimum dilution range. For example, Ti-15Mo alloy requires higher values of dilution to achieve optimal conditions due to the refractory nature of the material. Wherever no information was given about the optimal dilution values, it was considered to have an optimal dilution of 10% to 30%. Qualitatively, if the dilution level goes above 30%, it might lead to keyholing or below 10% might lead to a lack of fusion, and both cases are considered to be outside the optimal processing range. Another region on the process map is identified, called the mixed-mode porosity region, that occurs due to the combination of both keyholing and a lack of fusion. The high linear heat input is excessive for the upper layers of the powders, but due to the high feed rate, the heat input does not melt the bottom layers very efficiently (shielding by the powders). As a result, the top powder volume experiences keyholing and the bottom powder volume experiences a lack of fusion. A gas tungsten arc welding study defined this mid-porosity region in the literature [125]. This unique resemblance can be attributed towards the similarities between the welding and DED processes.

Table 5. Compilation of optimal processing data point ranges for DED deposited metal or alloy systems.

Material System	Optimal Dilution Range or Optimal Process Parameters or Acceptable Range Values as Reported	Study
Stainless steel grade 303L	–	[126]
H13 tool steel	Optimal, generally low dilution preferred	[12]
Inconel 718 in steel substrate	–	[127]
Ti-6Al-4V	Within 10%–30%	[128]
Ti-6Al-4V	–	[5]
H13 tool steel	–	[129]
P420 steel on low carbon steel	12%–20%; optimal is 16%	[130]
Inconel 690 on Inconel 600	Optimal	[131]
24CrMoNi alloy steel	32%	[2]
Ti-15Mo	54%–68%	[132]
Fe	10%–20%	[133]
Inconel 718 on AISI 1045 carbon steel	–	[83]
Stellite® 12 (Cr-W based alloy) on 0.2% C steel	–	[134]
Zirconium on Zr alloy	50%	[135]
Ti-6Al-4V	48%–52%	[136]
NiFeBSiNb on mild steel	Above 10%	[137]
Inconel	Optimal	[121]
Fe	–	[138]
Ti-6Al-4V	Within 10% to 30%	[128]
Ti-6Al-4V	Zero porosity data; optimal	[139]
NiCrAlY on Inconel 738 superalloy	15%–25%	[140]
Ni-Cr based alloy (commercially known as 19E alloy)	5%–30%	[141]

The graph shown in Figure 7 gives the optimal processing ranges for the alloy systems, like Inconel, Ti-6Al-4V, H13 Tool steel, Fe, Ti-15Mo, and some Ni-Cr alloys. From the graph, three regions which do not contain any optimal data points are observed. It can be hypothesized that these regions are due to three modes of increased porosity formation in the material: Keyholing (due to a high linear heat input and low powder feed rate), lack of fusion (due to a low linear heat input and high powder feed rate), and mid porosity zone (due to an appreciably high linear heat input and high powder feed rate contributing to mixed-mode porosity). These regions have been defined up to a linear heat input of 400 J/mm and a powder feed rate up to 25 g/min. Such regions are valid for most of the metal-alloy systems that have been studied.

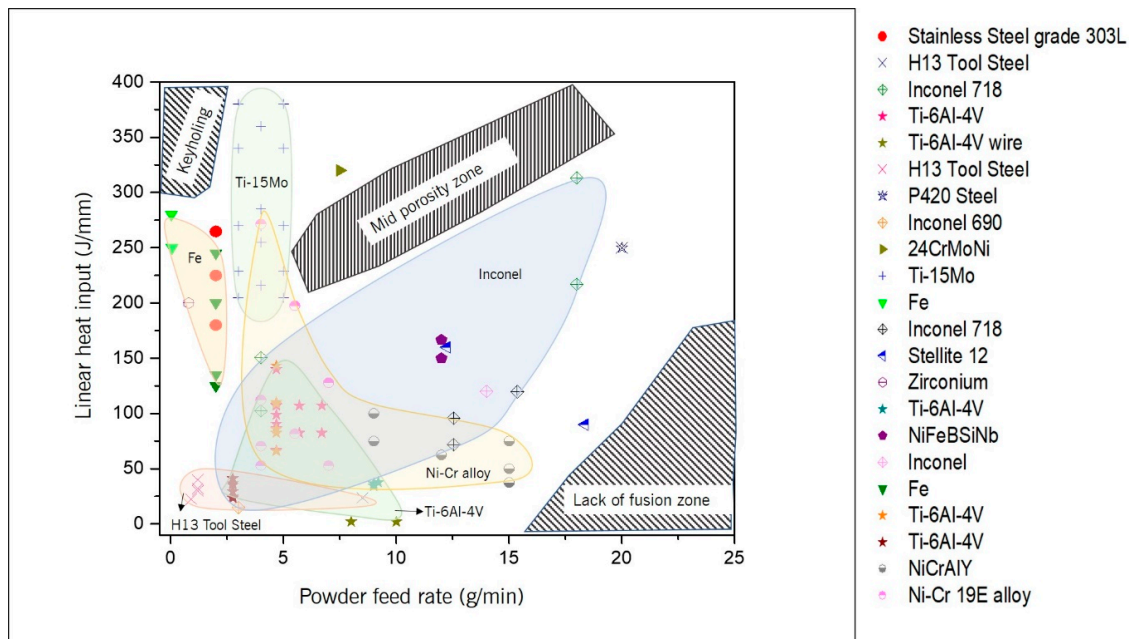


Figure 7. Optimal processing regions for Ti-6Al-4V, Inconel 690-718, Ni-Cr based alloys, Fe, H13 tool steel, and Ti-15Mo alloy, along with the unsuitable processing zones, as compiled in Table 5.

7. Applications and Emerging Technologies

This paper discussed the physics of DED technology and established process maps, which will be useful in various research fields as well as industries. This section lists some applications, both common in other metal AM techniques, as well as ones which are unique to DED, aiding the readers to understand the diverse functionalities of DED.

7.1. DED Metal Parts Used in Various Biomedical Applications

It is advantageous to produce porous implants using DED as compared to conventional casting methods: It is possible to alter the mechanical properties simply by changing the orientation or geometry of the build; it is possible to incorporate different materials together and obtain the optimal properties through a functionally graded material; and it is much easier to custom build the implants due to specific patient requirements. The most common materials used for biomedical applications are Ti and its alloys, Co based alloys, 316L stainless steel, and Ni-Ti based alloys. Additive manufactured parts have gained prominence in the orthopedic and dental implant industry. Biomedical applications garnered a revenue of 16.4% of the total AM industry in 2012 [10]. This shows promising metal DED applications in the biomedical industry, with a growing trend in the future, specifically in dental [142], orthopedic, and cardiovascular [143] applications. Biocompatibility tests on porous Ti-6Al-4V made with LENS™ proved the capability of cell growth on implants having a pore size of 200 μm or larger [144]. Also, in-vivo biocompatibility studies with porous Ti-6Al-4V processed by DED showed

that a pore volume fraction of 0.40 (upper limit) can accelerate the healing process through biological fixation [144].

7.2. Welding and Cladding

Conventional welding leads to high RS at the interfaces, especially for the welding of dissimilar metals. This might lead to early failures, and the results could be catastrophic. DED can be used to change the composition as a function of the position, facilitating a smooth transition from one joint to the other. This could be achieved by designing a gradient path that avoids the unwanted phases determined from multi-component phase diagrams [145]. This will reduce the RS and improve the mechanical integrity of the joints [146–152]. Cladding is generally used to form corrosion resistant protective coatings on substrates or to improve the tribological properties [56,153,154]. There is also an added advantage of using DED for cladding two dissimilar materials, due to the possibility of using functionally graded alloys. Another useful cladding technique is multi-axis cladding, making it possible to deposit layers at any angular axis. This functionality is a great advantage of DED over other AM systems [56,155–157].

7.3. Repair

Repairing (or remanufacturing) is essential to improve the life cycle of parts and to restore their functionality. This also leads to a reduced environmental impact, due to less material and energy wastage [12,13]. DED is a well-known repair technique, with the parts possessing good metallurgical bonding and exhibiting good post-repair mechanical properties [4,158]. Some studies establishing DED as a standard repairing technique in industries include: Repairing a gas-turbine blade using a Ni based superalloy delivered through a co-axial powder feeder [159]; repairing steam circuit parts at thermal power stations, using deposition of Co based alloys to maintain high temperature mechanical properties [160]; and repairing of Ti-6Al-4V aero engine parts using Ti-6Al-4V powders [161].

7.4. Bulk Combinatorial Alloy Design

It is possible to design alloys with compositional gradients using DED and this functionality is a unique characteristic which distinguishes DED from other AM systems. For example, the Ti-6Al-4V to V gradient and 304L steel to Invar 36 gradient were processed in the literature using DED. The aim was to successfully design the gradient path such that the unwanted brittle phases could be avoided in the microstructure, which would eventually give better mechanical properties for the printed parts [145]. This was done using multi-component phase diagrams. Another study used Cr-V-Mo hot working tool steel and Ni based maraging steel as base materials, with varying ratios of these two materials [162]. It was hot rolled and subsequently characterized, enabling high throughput probing of important alloy blends. DED processed high entropy alloy (HEA) AlCrFeMoV x ($x = 0$ to 1) was also studied in literature, to assess the composition–microstructure–hardness relationships [163]. High hardness was observed with increasing V, due to the high V solubility in this HEA leading to solid solution strengthening.

7.5. Construction Materials

AM, and in general DED, has good potential in the construction industry, but has its fair share of challenges, as structural members are usually quite big to be built using AM. Nonetheless, it would be advantageous to build highly specialized parts by exploiting this technology. Conventional casting leads to prismatic structures (uniform microstructures). With DED, engineered compositional and microstructural gradients in the structural parts are possible, which might give superior mechanical properties. An important thing to note is that the construction industry contributes to about 30% of greenhouse emissions in total, which could be reduced by partly adopting AM for the mass production of specialized parts [164].

7.6. Hybrid Additive Manufacturing

DED printed parts have several problems associated with it, like RS, lack of surface finish, etc., and to address these challenges without separate post-processing, several hybrid AM systems have been developed. Hybrid CNC-AM systems fully integrate the capabilities of both additive and subtractive manufacturing, which can be further exploited to increase productivity and competitiveness in the market. The parts produced by this hybrid method are precise even when produced in large-scale, due to the post-processing techniques integrated into a single system, without the need for separate machining. Hybrid manufacturing is still a relatively new technology and requires a lot more research for acceptance into the market. Therefore, the most important steps to be taken in the direction of improvement of such machines would be process optimization strategies along with developments in software integration [165]. Other secondary processes that complement the performance of DED parts (to name a few) are: Inter-pass rolling [166] and Ultrasonic Vibration Assisted LENS™ [167], both used for grain size refinement to enhance the mechanical properties of the parts.

8. Summary and Outlook

There are many far-from-equilibrium and highly dynamic phenomena during DED due to extreme heating and cooling rates. These include dynamic melt pool, melting and vaporization of powder particles, rapid solidification, and phase transformation. Such transient events often result in a large scatter in mechanical properties of printed components due to many complex interactions, leading to unwanted phase transformations and grain structures, residual stresses, and porosities. Further studies on establishing a correlation between composition, process parameters (powder feed rate, laser power, and velocity), process signature (melt pool stability and dimensions), and the resultant microstructure, pore content, residual stresses, and macroscopic properties will be extremely beneficial to the advancement of this technology. It is expected that the process physics of alloy systems and composite systems would be different and future studies are required in each area both experimentally and computationally.

The major contribution in this paper was the establishment of process maps for DED, after compiling the available literature. Researchers will be able to use this map to predict their preferred operating ranges for different alloy classes, but further work is required to extend our study to more extensive material systems. Hybrid AM technologies were discussed toward the end of this paper. These are relatively new approaches to overcome some of the limitations of AM. Further research is required in this area to mature these technologies beyond the current state of the art.

Funding: This research received no external funding.

Conflicts of Interest: The authors declare no conflict of interest.

References

1. Mazumder, J. Design for metallic additive manufacturing machine with capability for “certify as you build”. *Procedia CIRP* **2015**, *36*, 187–192. [[CrossRef](#)]
2. Cao, L.; Chen, S.; Wei, M.; Guo, Q.; Liang, J.; Liu, C.; Wang, M. Effect of laser energy density on defects behavior of direct laser depositing 24CrNiMo alloy steel. *Opt. Laser Technol.* **2019**, *111*, 541–553. [[CrossRef](#)]
3. Khairallah, S.A.; Anderson, A.T.; Rubenchik, A.M.; King, W.E. Laser powder-bed fusion additive manufacturing: Physics of complex melt flow and formation mechanisms of pores, spatter, and denudation zones. *Acta Mater.* **2016**, *108*, 36–45. [[CrossRef](#)]
4. Thompson, S.M.; Bian, L.; Shamsaei, N.; Yadollahi, A. An overview of Direct Laser Deposition for additive manufacturing; Part I: Transport phenomena, modeling and diagnostics. *Addit. Manuf.* **2015**, *8*, 36–62. [[CrossRef](#)]
5. Caiazzo, F. Additive manufacturing by means of laser-aided directed metal deposition of titanium wire. *Int. J. Adv. Manuf. Technol.* **2018**, *96*, 2699–2707. [[CrossRef](#)]

6. DebRoy, T.; Wei, H.L.; Zuback, J.S.; Mukherjee, T.; Elmer, J.W.; Milewski, J.O.; Beese, A.M.; Wilson-Heid, A.; De, A.; Zhang, W. Additive manufacturing of metallic components—Process, structure and properties. *Prog. Mater. Sci.* **2018**, *92*, 112–224. [[CrossRef](#)]
7. Sames, W.J.; List, F.A.; Pannala, S.; Dehoff, R.R.; Babu, S.S. The Metallurgy and Processing Science of metal additive manufacturing. *Int. Mater. Rev.* **2016**, *61*, 315–360. [[CrossRef](#)]
8. Gorsse, S.; Hutchinson, C.; Gouné, M.; Banerjee, R. Additive manufacturing of metals: A brief review of the characteristic microstructures and properties of steels, Ti-6Al-4V and high-entropy alloys. *Sci. Technol. Adv. Mater.* **2017**, *18*, 584–610. [[CrossRef](#)]
9. Lewandowski, J.J.; Seifi, M. Metal Additive Manufacturing: A Review of Mechanical Properties. *Annu. Rev. Mater. Res.* **2016**, *46*, 151–186. [[CrossRef](#)]
10. Harun, W.S.W.; Kamariah, M.S.I.N.; Muhamad, N.; Ghani, S.A.C.; Ahmad, F.; Mohamed, Z. A review of powder additive manufacturing processes for metallic biomaterials. *Powder Technol.* **2018**, *327*, 128–151. [[CrossRef](#)]
11. Pinkerton, A.J.; Ul Haq Syed, W.; Li, L. An experimental and theoretical investigation of combined gas- and water-atomized powder deposition with a diode laser. *J. Laser Appl.* **2006**, *18*, 73–80. [[CrossRef](#)]
12. Shin, Y.C.; Bailey, N.; Katinas, C.; Tan, W. Predictive modeling capabilities from incident powder and laser to mechanical properties for laser directed energy deposition. *Comput. Mech.* **2018**, *61*, 617–636. [[CrossRef](#)]
13. Ramani, K.; Ramanujan, D.; Bernstein, W.Z.; Zhao, F.; Sutherland, J.; Handwerker, C.; Choi, J.-K.; Kim, H.; Thurston, D. Integrated Sustainable Life Cycle Design: A Review. *J. Mech. Des.* **2010**, *132*, 091004. [[CrossRef](#)]
14. Greer, C.; Nycz, A.; Noakes, M.; Richardson, B.; Post, B.; Kurfess, T.; Love, L. Introduction to the design rules for Metal Big Area Additive Manufacturing. *Addit. Manuf.* **2019**, *27*, 159–166. [[CrossRef](#)]
15. Heralić, A.; Christiansson, A.K.; Lennartson, B. Height control of laser metal-wire deposition based on iterative learning control and 3D scanning. *Opt. Lasers Eng.* **2012**, *50*, 1230–1241. [[CrossRef](#)]
16. Zhang, L.C.; Liu, Y.; Li, S.; Hao, Y. Additive Manufacturing of Titanium Alloys by Electron Beam Melting: A Review. *Adv. Eng. Mater.* **2018**, *20*, 1–16. [[CrossRef](#)]
17. Hofer, K. Arc based additive manufacturing of steel components—Comparison of wire- and powder based variants. *Weld. World* **2018**, *62*, 243–247. [[CrossRef](#)]
18. Moridi, A.; Hassani-Gangaraj, S.M.; Guagliano, M.; Dao, M. Cold spray coating: Review of material systems and future perspectives. *Surf. Eng.* **2014**, *30*, 369–395. [[CrossRef](#)]
19. Hassani-Gangaraj, M.; Veysset, D.; Champagne, V.K.; Nelson, K.A.; Schuh, C.A. Adiabatic shear instability is not necessary for adhesion in cold spray. *Acta Mater.* **2018**, *158*, 430–439. [[CrossRef](#)]
20. Zheng, B.; Topping, T.; Smugeresky, J.E.; Zhou, Y.; Biswas, A.; Baker, D.; Lavernia, E.J. The influence of Ni-coated TiC on laser-deposited IN625 metal matrix composites. *Metall. Mater. Trans. A* **2010**, *41*, 568–573. [[CrossRef](#)]
21. Li, X.C.; Stampfl, J.; Prinz, F.B. Mechanical and thermal expansion behavior of laser deposited metal matrix composites of Invar and TiC. *Mater. Sci. Eng. A* **2002**, *282*, 86–90. [[CrossRef](#)]
22. Liu, W.; DuPont, J.N. Fabrication of carbide-particle-reinforced titanium aluminide-matrix composites by laser-engineered net shaping. *Metall. Mater. Trans. A* **2004**, *35*, 1133–1140. [[CrossRef](#)]
23. Liu, W.; DuPont, J.N. Fabrication of functionally graded TiC/Ti composites by Laser Engineered Net Shaping. *Scr. Mater.* **2003**, *48*, 1337–1342. [[CrossRef](#)]
24. Gualtieri, T.; Bandyopadhyay, A. Additive manufacturing of compositionally gradient metal-ceramic structures: Stainless steel to vanadium carbide. *Mater. Des.* **2018**, *139*, 419–428. [[CrossRef](#)]
25. Zhang, Y.; Bandyopadhyay, A. Direct fabrication of compositionally graded Ti-Al₂O₃ multi-material structures using Laser Engineered Net Shaping. *Addit. Manuf.* **2018**, *21*, 104–111. [[CrossRef](#)]
26. Balla, V.K.; DeVasConCellos, P.D.; Xue, W.; Bose, S.; Bandyopadhyay, A. Fabrication of compositionally and structurally graded Ti-TiO₂ structures using laser engineered net shaping (LENS). *Acta Biomater.* **2009**, *5*, 1831–1837. [[CrossRef](#)] [[PubMed](#)]
27. Bandyopadhyay, P.P.; Balla, V.K.; Bose, S.; Bandyopadhyay, A. Compositionally graded aluminum oxide coatings on stainless steel using laser processing. *J. Am. Ceram. Soc.* **2007**, *90*, 1989–1991. [[CrossRef](#)]
28. Das, M.; Balla, V.K.; Kumar, T.S.S.; Manna, I. Fabrication of Biomedical Implants using Laser Engineered Net Shaping (LENS™). *Trans. Indian Ceram. Soc.* **2013**, *72*, 169–174. [[CrossRef](#)]
29. Heer, B.; Bandyopadhyay, A. Silica coated titanium using Laser Engineered Net Shaping for enhanced wear resistance. *Addit. Manuf.* **2018**, *23*, 303–311. [[CrossRef](#)]

30. Das, M.; Balla, V.K.; Kumar, T.S.S.; Bandyopadhyay, A.; Manna, I. Tribological, electrochemical and in vitro biocompatibility properties of SiC reinforced composite coatings. *Mater. Des.* **2016**, *95*, 510–517. [[CrossRef](#)]
31. Bandyopadhyay, A.; Dittrick, S.; Gualtieri, T.; Wu, J.; Bose, S. Calcium phosphate-titanium composites for articulating surfaces of load-bearing implants. *J. Mech. Behav. Biomed. Mater.* **2016**, *57*, 280–288. [[CrossRef](#)] [[PubMed](#)]
32. Stenberg, K.; Dittrick, S.; Bose, S.; Bandyopadhyay, A. Influence of simultaneous addition of carbon nanotubes and calcium phosphate on wear resistance of 3D-printed Ti6Al4V. *J. Mater. Res.* **2018**, *33*, 2077–2086. [[CrossRef](#)]
33. Traxel, K.D.; Bandyopadhyay, A. Reactive-deposition based additive manufacturing of Ti-Zr-BN composites. *Addit. Manuf.* **2018**, *24*, 353–363. [[CrossRef](#)]
34. Ke, D.; Vu, A.A.; Bandyopadhyay, A.; Bose, S. Compositionally graded doped hydroxyapatite coating on titanium using laser and plasma spray deposition for bone implants. *Acta Biomater.* **2019**, *84*, 414–423. [[CrossRef](#)] [[PubMed](#)]
35. Torgerson, T.B.; Mantri, S.A.; Banerjee, R.; Scharf, T.W. Room and elevated temperature sliding wear behavior and mechanisms of additively manufactured novel precipitation strengthened metallic composites. *Wear* **2019**, *426*, 942–951. [[CrossRef](#)]
36. Srinivas, V.; Savitha, U.; Jagan Reddy, G. Processing and Characterization of NiCr-YSZ Compositionally Graded Coatings on Superalloy using Laser Engineered Net Shaping (LENS). *Mater. Today Proc.* **2018**, *5*, 27277–27284. [[CrossRef](#)]
37. Hu, Y.; Wang, H.; Li, Y.; Ning, F.; Cong, W. Surface grinding of ZTA parts fabricated by laser engineered net shaping process: Effects of ZrO₂ content and ultrasonic vibration. In Proceedings of the 13th International Manufacturing Science and Engineering Conference, College Station, TX, USA, 18–22 June 2018.
38. Yan, J.; Masoudi, N.; Battiato, I.; Fadel, G. Optimization of process parameters in laser engineered Net shaping (LENS) deposition of multi-materials. In Proceedings of the ASME 2015 International Design Engineering Technical Conferences and Computers and Information in Engineering Conference, Boston, MA, USA, 2–5 August 2015; p. V01AT02A034.
39. Zhang, Y.; Sahasrabudhe, H.; Bandyopadhyay, A. Additive manufacturing of Ti-Si-N ceramic coatings on titanium. *Appl. Surf. Sci.* **2015**, *346*, 428–437. [[CrossRef](#)]
40. Bernard, S.A.; Balla, V.K.; Bose, S.; Bandyopadhyay, A. Direct laser processing of bulk lead zirconate titanate ceramics. *Mater. Sci. Eng. B* **2010**, *172*, 85–88. [[CrossRef](#)]
41. Li, Y.; Hu, Y.; Cong, W.; Zhi, L.; Guo, Z. Additive manufacturing of alumina using laser engineered net shaping: Effects of deposition variables. *Ceram. Int.* **2017**, *43*, 7768–7775. [[CrossRef](#)]
42. Niu, F.; Wu, D.; Zhou, S.; Ma, G. Power prediction for laser engineered net shaping of Al₂O₃ ceramic parts. *J. Eur. Ceram. Soc.* **2014**, *34*, 3811–3817. [[CrossRef](#)]
43. Wu, D.J.; Niu, F.Y.; Ma, G.Y.; Zhang, B.; Yan, S. Process optimization for suppressing cracks in laser engineered net shaping of Al₂O₃ ceramics. *JOM* **2016**, *69*, 557–562.
44. Ma, G.; Wang, J.; Niu, F.; Sun, B.; Wu, D. Influence of powder distribution on the Al₂O₃ thin-wall ceramic formed by laser engineered net shaping. *Chin. J. Lasers* **2015**, *42*, 0103006.
45. Niu, F.; Wu, D.; Ma, G.; Zhang, B. Additive manufacturing of ceramic structures by laser engineered net shaping. *Chin. J. Mech. Eng.* **2015**, *28*, 1117–1122. [[CrossRef](#)]
46. Wu, D.; Liu, H.; Lu, F.; Ma, G.; Yan, S.; Niu, F.; Guo, D. Al₂O₃-YAG eutectic ceramic prepared by laser additive manufacturing with water-cooled substrate. *Ceram. Int.* **2019**, *45*, 4119–4122. [[CrossRef](#)]
47. Roy, M.; Vamsi Krishna, B.; Bandyopadhyay, A.; Bose, S. Laser processing of bioactive tricalcium phosphate coating on titanium for load-bearing implants. *Acta Biomater.* **2008**, *4*, 324–333. [[CrossRef](#)] [[PubMed](#)]
48. Yan, S.; Wu, D.; Niu, F.; Huang, Y.; Liu, N.; Ma, G. Effect of ultrasonic power on forming quality of nano-sized Al₂O₃-ZrO₂ eutectic ceramic via laser engineered net shaping (LENS). *Ceram. Int.* **2018**, *44*, 1120–1126. [[CrossRef](#)]
49. Hu, Y.; Ning, F.; Cong, W.; Li, Y.; Wang, X.; Wang, H. Ultrasonic vibration-assisted laser engineering net shaping of ZrO₂-Al₂O₃ bulk parts: Effects on crack suppression, microstructure, and mechanical properties. *Ceram. Int.* **2018**, *44*, 2752–2760. [[CrossRef](#)]
50. Niu, F.; Wu, D.; Ma, G.; Wang, J.; Guo, M.; Zhang, B. Nanosized microstructure of Al₂O₃-ZrO₂ (Y₂O₃) eutectics fabricated by laser engineered net shaping. *Scr. Mater.* **2015**, *95*, 39–41. [[CrossRef](#)]
51. Marattukalam, J.J.; Singh, A.K.; Datta, S.; Das, M.; Balla, V.K.; Bontha, S.; Kalpathy, S.K. Microstructure and corrosion behavior of laser processed NiTi alloy. *Mater. Sci. Eng. C* **2015**, *57*, 309–313. [[CrossRef](#)]

52. Stull, J.A.; Hill, M.A.; Lienert, T.J.; Tokash, J.; Bohn, K.R.; Hooks, D.E. Corrosion characteristics of laser-engineered net shaping additively-manufactured 316L stainless steel. *JOM* **2018**, *70*, 2677–2683. [[CrossRef](#)]
53. Dehoff, R.R.; Sarosi, P.M.; Collins, P.C.; Fraser, H.L.; Mills, M.J. Microstructural evaluation of LENS™ deposited Nb-Ti-Si-Cr alloys. *MRS Online Proc. Libr. Arch.* **2002**, *753*, 2–7. [[CrossRef](#)]
54. Sridharan, N.; Cakmak, E.; Dehoff, R.R. Microstructure evolution during laser direct energy deposition of a novel Fe-Cr-Ni-W-B hardfacing coating. *Surf. Coat. Technol.* **2019**, *358*, 362–370. [[CrossRef](#)]
55. Gu, D.D.; Meiners, W.; Wissenbach, K.; Poprawe, R. Laser additive manufacturing of metallic components: Materials, processes and mechanisms. *Int. Mater. Rev.* **2012**, *57*, 133–164. [[CrossRef](#)]
56. Gibson, I.; Rosen, D.; Stucker, B. *Additive Manufacturing Technologies: 3D Printing, Rapid Prototyping, and Direct Digital Manufacturing*, 2nd ed.; Springer: New York, NY, USA, 2015.
57. DebRoy, T.; Zhang, W.; Turner, J.; Babu, S.S. Building digital twins of 3D printing machines. *Scr. Mater.* **2017**, *135*, 119–124. [[CrossRef](#)]
58. Pinkerton, A.J.; Moat, R.; Shah, K.; Li, L.; Preuss, M.; Withers, P.J. A verified model of laser direct metal deposition using an analytical enthalpy balance method. In Proceedings of the International Congress on Applications of Lasers & Electro-Optics, Orlando, FL, USA, 29 October–1 November 2007.
59. Liu, S.; Zhang, Y.; Kovacevic, R. Numerical simulation and experimental study of powder flow distribution in high power direct diode laser cladding process. *Lasers Manuf. Mater. Process.* **2015**, *2*, 199–218. [[CrossRef](#)]
60. Heigel, J.C.; Michaleris, P.; Reutzel, E.W. Thermo-mechanical model development and validation of directed energy deposition additive manufacturing of Ti-6Al-4V. *Addit. Manuf.* **2015**, *5*, 9–19. [[CrossRef](#)]
61. Kovaleva, I.; Kovalev, O.; Zaitsev, A.; Smurov, I. Numerical simulation and comparison of powder jet profiles for different types of coaxial nozzles in direct material deposition. *Phys. Procedia* **2013**, *41*, 870–872. [[CrossRef](#)]
62. Tian, Y.; McAllister, D.; Colijn, H.; Mills, M.; Farson, D.; Nordin, M.; Babu, S. Rationalization of microstructure heterogeneity in INCONEL 718 builds made by the direct laser additive manufacturing process. *Metall. Mater. Trans. A Phys. Metall. Mater. Sci.* **2014**, *45*, 4470–4483. [[CrossRef](#)]
63. Radhakrishnan, B.; Gorti, S.; Babu, S. Large scale phase field simulations of microstructure evolution during thermal cycling. In Proceedings of the International Conference on Solid-Solid Phase Transformations in Inorganic Materials (PTM), Whistler, BC, Canada, 28 June–3 July 2015.
64. Amine, T.; Newkirk, J.W.; Liou, F. Investigation of effect of process parameters on multilayer builds by direct metal deposition. *Appl. Therm. Eng.* **2014**, *73*, 500–511. [[CrossRef](#)]
65. DebRoy, T.; David, S.A. Physical processes in fusion welding. *Rev. Mod. Phys.* **1995**, *67*, 85–112. [[CrossRef](#)]
66. Raghavan, A.; Wei, H.L.; Palmer, T.A.; DebRoy, T. Heat transfer and fluid flow in additive manufacturing. *J. Laser Appl.* **2014**, *25*, 052006. [[CrossRef](#)]
67. Manvatkar, V.; De, A.; DebRoy, T. Spatial variation of melt pool geometry, peak temperature and solidification parameters during laser assisted additive manufacturing process. *Mater. Sci. Technol.* **2015**, *31*, 924–930. [[CrossRef](#)]
68. Manvatkar, V.; De, A.; Debroy, T. Heat transfer and material flow during laser assisted multi-layer additive manufacturing. *J. Appl. Phys.* **2014**, *116*, 124905. [[CrossRef](#)]
69. Farahmand, P.; Kovacevic, R. An experimental–numerical investigation of heat distribution and stress field in single- and multi-track laser cladding by a high-power direct diode laser. *Opt. Laser Technol.* **2014**, *63*, 154–168. [[CrossRef](#)]
70. Cao, J.; Gharghoury, M.A.; Nash, P. Finite-element analysis and experimental validation of thermal residual stress and distortion in electron beam additive manufactured Ti-6Al-4V build plates. *J. Mater. Process. Technol.* **2016**, *237*, 409–419. [[CrossRef](#)]
71. Heiple, C.R.; Roper, J.R.; Stagner, R.T.; Aden, R.J. Surface active element effects on the shape of GTA, laser and electron beam welds. *Weld. J.* **1983**, *62*, 72–77.
72. Mills, K.C.; Keene, B.J.; Brooks, R.F.; Shirali, A. Marangoni effects in welding. *Philos. Trans. R. Soc. A Math. Phys. Eng. Sci.* **1998**, *356*, 911–925. [[CrossRef](#)]
73. Aucott, L.; Dong, H.; Mirihanage, W.; Atwood, R.; Kidess, A.; Gao, S.; Wen, S.; Marsden, J.; Feng, S.; Tong, M.; et al. Revealing internal flow behaviour in arc welding and additive manufacturing of metals. *Nat. Commun.* **2018**, *9*, 1–7. [[CrossRef](#)]
74. Mukherjee, T.; Manvatkar, V.; De, A.; DebRoy, T. Dimensionless numbers in additive manufacturing. *J. Appl. Phys.* **2017**, *121*, 024904. [[CrossRef](#)]

75. Van Elsen, M.; Al-Bender, F.; Kruth, J.P. Application of dimensional analysis to selective laser melting. *Rapid Prototyp. J.* **2008**, *14*, 15–22. [[CrossRef](#)]
76. Mukherjee, T.; Manvatkar, V.; De, A.; DebRoy, T. Mitigation of thermal distortion during additive manufacturing. *Scr. Mater.* **2017**, *127*, 79–83. [[CrossRef](#)]
77. Lia, F.; Park, J.; Tressler, J.; Martukanitz, R. Partitioning of laser energy during directed energy deposition. *Addit. Manuf.* **2017**, *18*, 31–39. [[CrossRef](#)]
78. Song, J.; Chew, Y.; Bi, G.; Yao, X.; Zhang, B.; Bai, J.; Moon, S.K. Numerical and experimental study of laser aided additive manufacturing for melt-pool profile and grain orientation analysis. *Mater. Des.* **2018**, *137*, 286–297. [[CrossRef](#)]
79. Bontha, S.; Klingbeil, N.W.; Kobryn, P.A.; Fraser, H.L. Thermal process maps for predicting solidification microstructure in laser fabrication of thin-wall structures. *J. Mater. Process. Technol.* **2006**, *178*, 135–142. [[CrossRef](#)]
80. Liu, P.; Wang, Z.; Xiao, Y.; Horstemeyer, M.F.; Cui, X.; Chen, L. Insight into the mechanisms of columnar to equiaxed grain transition during metallic additive manufacturing. *Addit. Manuf.* **2019**, *26*, 22–29. [[CrossRef](#)]
81. Marshall, G.J.; Young, W.J.; Thompson, S.M.; Shamsaei, N.; Daniewicz, S.R.; Shao, S. Understanding the microstructure formation of Ti-6Al-4V during direct laser deposition via in-situ thermal monitoring. *JOM* **2016**, *68*, 778–790. [[CrossRef](#)]
82. Kistler, N.A.; Corbin, D.J.; Nassar, A.R.; Reutzel, E.W.; Beese, A.M. Effect of processing conditions on the microstructure, porosity, and mechanical properties of Ti-6Al-4V repair fabricated by directed energy deposition. *J. Mater. Process. Technol.* **2019**, *264*, 172–181. [[CrossRef](#)]
83. Wolff, S.J. *Laser-Matter Interactions in Directed Energy Deposition*; Northwestern University Press: Evanston, IL, USA, 2018.
84. Spalding, I.J. Applied laser tooling. *J. Mod. Opt.* **2007**, *35*, 754–755. [[CrossRef](#)]
85. Wolff, S.J.; Lin, S.; Faierson, E.J.; Liu, W.K.; Wagner, G.J.; Cao, J. A framework to link localized cooling and properties of directed energy deposition (DED)-processed Ti-6Al-4V. *Acta Mater.* **2017**, *132*, 106–117. [[CrossRef](#)]
86. Ahsan, M.N.; Bradley, R.; Pinkerton, A.J. Microcomputed tomography analysis of intralayer porosity generation in laser direct metal deposition and its causes. *J. Laser Appl.* **2011**, *23*, 022009. [[CrossRef](#)]
87. Cunningham, R.; Nicolas, A.; Madsen, J.; Fodran, E.; Anagnostou, E.; Sangid, M.D.; Rollett, A. Analyzing the effects of powder and post-processing on porosity and properties of electron beam melted Ti-6Al-4V. *Mater. Res. Lett.* **2017**, *5*, 516–525. [[CrossRef](#)]
88. Rabin, B.H.; Smolik, G.R.; Korth, G.E. Characterization of entrapped gases in rapidly solidified powders. *Mater. Sci. Eng. A* **1990**, *124*, 1–7. [[CrossRef](#)]
89. Wang, Z.; Denlinger, E.; Michaleris, P.; Stoica, A.D.; Ma, D.; Beese, A.M. Residual stress mapping in Inconel 625 fabricated through additive manufacturing: Method for neutron diffraction measurements to validate thermomechanical model predictions. *Mater. Des.* **2017**, *113*, 169–177. [[CrossRef](#)]
90. Rafi, H.K.; Pal, D.; Patil, N.; Starr, T.L.; Stucker, B.E. Microstructure and Mechanical Behavior of 17-4 Precipitation Hardenable Steel Processed by Selective Laser Melting. *J. Mater. Eng. Perform.* **2014**, *23*, 4421–4428. [[CrossRef](#)]
91. Wang, Z.; Beese, A.M. Effect of chemistry on martensitic phase transformation kinetics and resulting properties of additively manufactured stainless steel. *Acta Mater.* **2017**, *131*, 410–422. [[CrossRef](#)]
92. Mukherjee, T.; Zuback, J.S.; De, A.; DebRoy, T. Printability of alloys for additive manufacturing. *Sci. Rep.* **2016**, *6*, 1–8. [[CrossRef](#)] [[PubMed](#)]
93. Sandgren, H.R.; Zhai, Y.; Lados, D.A.; Shade, P.A.; Schuren, J.C.; Groeber, M.A.; Kenesei, P.; Gavras, A.G. Characterization of fatigue crack growth behavior in LENS fabricated Ti-6Al-4V using high-energy synchrotron x-ray microtomography. *Addit. Manuf.* **2016**, *12*, 132–141. [[CrossRef](#)]
94. Beese, A.M.; Carroll, B.E. Review of mechanical properties of Ti-6Al-4V made by laser based additive manufacturing using powder feedstock. *JOM* **2016**, *68*, 724–734. [[CrossRef](#)]
95. Carroll, B.E.; Palmer, T.A.; Beese, A.M. Anisotropic tensile behavior of Ti-6Al-4V components fabricated with directed energy deposition additive manufacturing. *Acta Mater.* **2015**, *87*, 309–320. [[CrossRef](#)]
96. Shamsaei, N.; Yadollahi, A.; Bian, L.; Thompson, S.M. An overview of direct laser deposition for additive manufacturing; Part II: Mechanical behavior, process parameter optimization and control. *Addit. Manuf.* **2015**, *8*, 12–35. [[CrossRef](#)]

97. Zuback, J.S.; DebRoy, T. The Hardness of Additively Manufactured Alloys. *Materials* **2018**, *11*, 2070. [[CrossRef](#)] [[PubMed](#)]
98. Arcella, F.G.; Froes, F.H. Producing titanium aerospace components from powder using laser forming. *JOM* **2000**, *52*, 28–30. [[CrossRef](#)]
99. Kobryn, P.A.; Semiatin, S.L. *Mechanical Properties of Laser-Deposited Ti-6Al-4V*; Air Force Research Laboratory: Hanscom, MA, USA, 2013.
100. Zhai, Y.; Galarraga, H.; Lados, D.A. Microstructure evolution, tensile properties, and fatigue damage mechanisms in Ti-6Al-4V alloys fabricated by two additive manufacturing techniques. *Procedia Eng.* **2015**, *114*, 658–666. [[CrossRef](#)]
101. Bian, L.; Thompson, S.M.; Shamsaei, N. Mechanical properties and microstructural features of direct laser-deposited Ti-6Al-4V. *JOM* **2015**, *67*, 629–638. [[CrossRef](#)]
102. Nalla, R.K.; Ritchie, R.O.; Boyce, B.L.; Campbell, J.P.; Peters, J.O. Influence of microstructure on high-cycle fatigue of Ti-6Al-4V: Bimodal vs. lamellar structures. *Metall. Mater. Trans. A* **2002**, *33*, 899–918. [[CrossRef](#)]
103. Prabhu, A.W.; Vincent, T.; Chaudhary, A.; Zhang, W.; Babu, S.S. Effect of microstructure and defects on fatigue behaviour of directed energy deposited Ti-6Al-4V. *Sci. Technol. Weld. Join.* **2015**, *20*, 659–669. [[CrossRef](#)]
104. Kobryn, P.A.; Semiatin, S. Mechanical properties of laser-deposited Ti-6Al-4V. In *Solid Freeform Fabrication Proceedings*; Landes Bioscience: Austin, TX, USA, 2001.
105. Zhai, Y.; Lados, D.A.; Brown, E.J.; Vigilante, G.N. Fatigue crack growth behavior and microstructural mechanisms in Ti-6Al-4V manufactured by laser engineered net shaping. *Int. J. Fatigue* **2016**, *93*, 51–63. [[CrossRef](#)]
106. Li, C.; Liu, Z.Y.; Fang, X.Y.; Guo, Y.B. Residual stress in metal additive manufacturing. *Procedia CIRP* **2018**, *71*, 348–353. [[CrossRef](#)]
107. NIST. *Measurement Science for Additive Manufacturing Program*; NIST: Gaithersburg, MD, USA, 2013.
108. Kenel, C.; Grolimund, D.; Li, X.; Panepucci, E.; Samson, V.A.; Sanchez, D.F.; Marone, F.; Leinenbach, C. In situ investigation of phase transformations in Ti-6Al-4V under additive manufacturing conditions combining laser melting and high-speed micro-X-ray diffraction. *Sci. Rep.* **2017**, *7*, 1–10. [[CrossRef](#)]
109. Wolff, S.J.; Wu, H.; Parab, N.; Zhao, C.; Ehmann, K.F.; Sun, T.; Cao, J. In-situ high-speed X-ray imaging of piezo-driven directed energy deposition additive manufacturing. *Sci. Rep.* **2019**, *9*, 1–14. [[CrossRef](#)]
110. Koester, L.W.; Taheri, H.; Bigelow, T.A.; Bond, L.J.; Faierson, E.J. In-situ acoustic signature monitoring in additive manufacturing processes. *AIP Conf. Proc.* **2018**, *1949*, 020006. [[CrossRef](#)]
111. Wang, F.; Mao, H.; Zhang, D.; Zhao, X.; Shen, Y. Online study of cracks during laser cladding process based on acoustic emission technique and finite element analysis. *Appl. Surf. Sci.* **2008**, *255*, 3267–3275. [[CrossRef](#)]
112. Griffith, M.L.; Schlienger, M.E.; Harwell, L.D.; Oliver, M.S.; Baldwin, M.D.; Ensz, M.T.; Essien, M.; Brooks, J.; Robino, C.V.; Smugeresky, J.E.; et al. Understanding thermal behavior in the LENS process. *Mater. Des.* **1999**, *20*, 107–113. [[CrossRef](#)]
113. Nassar, A.R.; Keist, J.S.; Reutzel, E.W.; Spurgeon, T.J. Intra-layer closed-loop control of build plan during directed energy additive manufacturing of Ti-6Al-4V. *Addit. Manuf.* **2015**, *6*, 39–52. [[CrossRef](#)]
114. Wang, L.; Felicelli, S.D.; Craig, J.E. Thermal modeling and experimental validation in the LENS™ process. In *Proceedings of the 18th Solid Freeform Fabrication Symposium*, Austin, TX, USA, 2007; pp. 100–111.
115. Hua, T.; Jing, C.; Xin, L.; Fengying, Z.; Weidong, H. Research on molten pool temperature in the process of laser rapid forming. *J. Mater. Process. Technol.* **2008**, *198*, 454–462. [[CrossRef](#)]
116. Tellez, A.G.M. *Fibre Laser Metal Deposition with Wire: Parameters Study and Temperature Control*; University of Nottingham: Nottingham, UK, 2010.
117. Yu, J.; Lin, X.; Wang, J.; Chen, J.; Huang, W. Mechanics and energy analysis on molten pool spreading during laser solid forming. *Appl. Surf. Sci.* **2010**, *256*, 4612–4620. [[CrossRef](#)]
118. Hu, D.; Kovacevic, R. Sensing, modeling and control for laser based additive manufacturing. *Int. J. Mach. Tools Manuf.* **2003**, *43*, 51–60. [[CrossRef](#)]
119. Gegel, M.L.; Bristow, D.A.; Landers, R.G. A Quadratic-optimal repetitive process controller for laser metal deposition. In *Proceedings of the Annual American Control Conference (ACC)*, Seattle, WA, USA, 27–29 June 2018.
120. Thomas, M.; Baxter, G.J.; Todd, I. Normalised model based processing diagrams for additive layer manufacture of engineering alloys. *Acta Mater.* **2016**, *108*, 26–35. [[CrossRef](#)]

121. Kuriya, T.; Ryo, K.; Oda, Y.; Yasuhiro, K. Evaluation and Analysis of Generated Void in Directed Energy Deposition of Inconel 718. *J. Jpn. Soc. Precis. Eng.* **2018**, *84*, 371–377. [[CrossRef](#)]
122. Ferguson, J.B.; Schultz, B.F.; Moghadam, A.D.; Rohatgi, P.K. Semi-empirical model of deposit size and porosity in 420 stainless steel and 4140 steel using laser engineered net shaping. *J. Manuf. Process.* **2015**, *19*, 163–170. [[CrossRef](#)]
123. Sciammarella, F.; Salehi Najafabadi, B. Processing Parameter DOE for 316L Using Directed Energy Deposition. *J. Manuf. Mater. Process.* **2018**, *2*, 61. [[CrossRef](#)]
124. Mahamood, R.M.; Akinlabi, E.T. Processing Parameters Optimization for Material Deposition Efficiency in Laser Metal Deposited Titanium Alloy. *Lasers Manuf. Mater. Process.* **2016**, *3*, 9–21. [[CrossRef](#)]
125. Ahsan, M.R.; Kim, Y.R.; Ashiri, R.; Cho, Y.J.; Jeong, C.; Park, Y.D. Cold metal transfer (CMT) gma of zinc-coated steel. *Weld. J.* **2016**, *95*, 120–132.
126. Fathi, A.; Toyserkani, E.; Khajepour, A.; Durali, M. Prediction of melt pool depth and dilution in laser powder deposition. *J. Phys. D Appl. Phys.* **2006**, *39*, 2613–2623. [[CrossRef](#)]
127. Bax, B.; Rajput, R.; Kellet, R.; Reisacher, M. Systematic evaluation of process parameter maps for laser cladding and directed energy deposition. *Addit. Manuf.* **2018**, *21*, 487–494. [[CrossRef](#)]
128. Fan, Z.; Jambunathan, A.; Sparks, T.E.; Ruan, J.; Yang, Y.; Bao, Y.; Liou, F. Numerical simulation and prediction of dilution during laser deposition. In *Solid Freeform Fabrication Proceedings, Proceedings of Seventeenth Annual Solid Freeform Fabrication (SFF) Symposium, Austin, TX, USA, 14–16 August 2006*; University of Texas at Austin: Austin, TX, USA, 2006; pp. 532–545.
129. Kong, F.; Kovacevic, R. Modeling of heat transfer and fluid flow in the laser multilayered cladding process. *Metall. Mater. Trans. B Process Metall. Mater. Process. Sci.* **2010**, *41*, 1310–1320. [[CrossRef](#)]
130. Saqiba, S.; Urbanica, R.J.; Aggarwal, K. Analysis of laser cladding bead morphology for developing additive manufacturing travel paths. *Procedia CIRP* **2014**, *17*, 824–829. [[CrossRef](#)]
131. Baidridge, T.; Poling, G.; Foroozmehr, E.; Kovacevic, R.; Metz, T.; Kadekar, V.; Gupta, M.C. Laser cladding of Inconel 690 on Inconel 600 superalloy for corrosion protection in nuclear applications. *Opt. Lasers Eng.* **2013**, *51*, 180–184. [[CrossRef](#)]
132. Bhardwaj, T.; Shukla, M.; Paul, C.P.; Bindra, K.S. Direct energy deposition-laser additive manufacturing of titanium-molybdenum alloy: Parametric studies, microstructure and mechanical properties. *J. Alloy. Compd.* **2019**, *787*, 1238–1248. [[CrossRef](#)]
133. Ansari, M.; Mohamadizadeh, A.; Huang, Y.; Paserin, V.; Toyserkani, E. Laser directed energy deposition of water-atomized iron powder: Process optimization and microstructure of single-tracks. *Opt. Laser Technol.* **2019**, *112*, 485–493. [[CrossRef](#)]
134. Hofman, J.T.; De Lange, D.F.; Pathiraj, B.; Meijer, J. FEM modeling and experimental verification for dilution control in laser cladding. *J. Mater. Process. Technol.* **2011**, *211*, 187–196. [[CrossRef](#)]
135. Harooni, A.; Nasiri, A.M.; Gerlich, A.P.; Khajepour, A.; Khalifa, A.; King, J.M. Processing window development for laser cladding of zirconium on zirconium alloy. *J. Mater. Process. Technol.* **2016**, *230*, 263–271. [[CrossRef](#)]
136. Sun, Y.; Hao, M. Statistical analysis and optimization of process parameters in Ti6Al4V laser cladding using Nd:YAG laser. *Opt. Lasers Eng.* **2012**, *50*, 985–995. [[CrossRef](#)]
137. Li, R.; Li, Z.; Huang, J.; Zhu, Y. Dilution effect on the formation of amorphous phase in the laser clad Ni-Fe-B-Si-Nb coatings after laser remelting process. *Appl. Surf. Sci.* **2012**, *258*, 7956–7961. [[CrossRef](#)]
138. Huang, Y.; Khamesee, M.B.; Toyserkani, E. A new physics based model for laser directed energy deposition (powder-fed additive manufacturing): From single-track to multi-track and multi-layer. *Opt. Laser Technol.* **2019**, *109*, 584–599. [[CrossRef](#)]
139. Kobryn, P.A.; Moore, E.H.; Semiatin, S.L. Effect of laser power and traverse speed on microstructure, porosity, and build height in laser-deposited Ti-6Al-4V. *Scr. Mater.* **2000**, *43*, 299–305. [[CrossRef](#)]
140. Ansari, M.; Shoja Razavi, R.; Barekat, M. An empirical-statistical model for coaxial laser cladding of NiCrAlY powder on Inconel 738 superalloy. *Opt. Laser Technol.* **2016**, *86*, 136–144. [[CrossRef](#)]
141. De Oliveira, U.; Ocelík, V.; De Hosson, J.T.M. Analysis of coaxial laser cladding processing conditions. *Surf. Coat. Technol.* **2005**, *197*, 127–136. [[CrossRef](#)]
142. Koike, M.; Martinez, K.; Guo, L.; Chahine, G.; Kovacevic, R.; Okabe, T. Evaluation of titanium alloy fabricated using electron beam melting system for dental applications. *J. Mater. Process. Technol.* **2011**, *211*, 1400–1408. [[CrossRef](#)]

143. Cui, Z.; Yang, B.; Li, R.K. Application of biomaterials in cardiac repair and regeneration. *Engineering* **2016**, *2*, 141–148. [[CrossRef](#)]
144. Xue, W.; Krishna, B.V.; Bandyopadhyay, A.; Bose, S. Processing and biocompatibility evaluation of laser processed porous titanium. *Acta Biomater.* **2007**, *3*, 1007–1018. [[CrossRef](#)] [[PubMed](#)]
145. Hofmann, D.C.; Roberts, S.; Otis, R.; Kolodziejska, J.; Dillon, R.P.; Suh, J.O.; Shapiro, A.A.; Liu, Z.K.; Borgonia, J.P. Developing gradient metal alloys through radial deposition additive manufacturing. *Sci. Rep.* **2014**, *4*, 5357. [[CrossRef](#)] [[PubMed](#)]
146. Korinko, P.; Adams, T. Laser engineered net shaping for repair and hydrogen compatibility. *Weld. J.* **2011**, *90*, 171–181.
147. Chaudhari, R.; Ingle, A.; Kalita, K. Stress Analysis of Dissimilar Metal Weld between Carbon Steel and Stainless Steel formed by Transition Grading Technique. *Mater. Today Proc.* **2015**, *2*, 1657–1664. [[CrossRef](#)]
148. Brentrup, G.; Leister, B.; Snowden, B.; DuPont, J.; Grenestedt, J. Preventing dissimilar metal weld failures: Application of new functionally graded transition joints. *Proc. Mater. Sci. Technol.* **2009**, *2009*, 2554–2562.
149. Sexton, L.; Lavin, S.; Byrne, G.; Kennedy, A. Laser cladding of aerospace materials. *J. Mater. Process. Technol.* **2002**, *122*, 63–68. [[CrossRef](#)]
150. Zhou, S.; Zeng, X.; Hu, Q.; Huang, Y. Analysis of crack behavior for Ni based WC composite coatings by laser cladding and crack-free realization. *Appl. Surf. Sci.* **2008**, *255*, 1646–1653. [[CrossRef](#)]
151. Mackwood, A.P.; Crafer, R.C. Thermal modelling of laser welding and related processes: A literature review. *Opt. Laser Technol.* **2005**, *37*, 99–115. [[CrossRef](#)]
152. Li, L. Advances and characteristics of high-power diode laser materials processing. *Opt. Lasers Eng.* **2000**, *34*, 231–253. [[CrossRef](#)]
153. Das, M.; Bhattacharya, K.; Dittrick, S.A.; Mandal, C.; Balla, V.K.; Sampath Kumar, T.S.; Bandyopadhyay, A.; Manna, I. In situ synthesized TiB-TiN reinforced Ti6Al4V alloy composite coatings: Microstructure, tribological and in-vitro biocompatibility. *J. Mech. Behav. Biomed. Mater.* **2014**, *29*, 259–271. [[CrossRef](#)] [[PubMed](#)]
154. Han, L.; Phatak, K.M.; Liou, F.W. Modeling of laser cladding with powder injection. *Metall. Mater. Trans. B* **2007**, *35*, 1139–1150. [[CrossRef](#)]
155. Paul, C.P.; Jain, A.; Ganesh, P.; Negi, J.; Nath, A.K. Laser rapid manufacturing of Colmonoy-6 components. *Opt. Lasers Eng.* **2006**, *44*, 1096–1109. [[CrossRef](#)]
156. Calleja, A.; Taberner, I.; Fernández, A.; Celaya, A.; Lamikiz, A.; López De Lacalle, L.N. Improvement of strategies and parameters for multi-axis laser cladding operations. *Opt. Lasers Eng.* **2014**, *56*, 113–120. [[CrossRef](#)]
157. Zhang, J.; Liou, F. Adaptive Slicing for a Multi-Axis Laser Aided Manufacturing Process. *J. Mech. Des.* **2004**, *126*, 254–261. [[CrossRef](#)]
158. Liu, Z.; Cong, W.; Kim, H.; Ning, F.; Jiang, Q.; Li, T.; Zhang, H.C.; Zhou, Y. Feasibility exploration of superalloys for AISI 4140 steel repairing using laser engineered net shaping. *Procedia Manuf.* **2017**, *10*, 912–922. [[CrossRef](#)]
159. Bi, G.; Gasser, A. Restoration of nickel-base turbine blade knife-edges with controlled laser aided additive manufacturing. *Phys. Procedia* **2011**, *12*, 402–409. [[CrossRef](#)]
160. Díaz, E.; Amado, J.M.; Montero, J.; Tobar, M.J.; Yáñez, A. Comparative study of Co based alloys in repairing low Cr-Mo steel components by laser cladding. *Phys. Procedia* **2012**, *39*, 368–375. [[CrossRef](#)]
161. Raju, R.; Duraiselvam, M.; Petley, V.; Verma, S.; Rajendran, R. Microstructural and mechanical characterization of Ti6Al4V refurbished parts obtained by laser metal deposition. *Mater. Sci. Eng. A* **2015**, *643*, 64–71. [[CrossRef](#)]
162. Knoll, H.; Ocylok, S.; Weisheit, A.; Springer, H.; Jäggle, E.; Raabe, D. Combinatorial Alloy Design by Laser Additive Manufacturing. *Steel Res. Int.* **2017**, *88*, 1–11. [[CrossRef](#)]
163. Gwalani, B.; Soni, V.; Waseem, O.A.; Mantri, S.A.; Banerjee, R. Laser additive manufacturing of compositionally graded AlCrFeMoVx ($x = 0$ to 1) high-entropy alloy system. *Opt. Laser Technol.* **2019**, *113*, 330–337. [[CrossRef](#)]
164. Buchanan, C.; Gardner, L. Metal 3D printing in construction: A review of methods, research, applications, opportunities and challenges. *Eng. Struct.* **2019**, *180*, 332–348. [[CrossRef](#)]
165. Cortina, M.; Arrizubieta, J.I.; Ruiz, J.E.; Ukar, E.; Lamikiz, A. Latest developments in industrial hybrid machine tools that combine additive and subtractive operations. *Materials* **2018**, *11*, 2583. [[CrossRef](#)] [[PubMed](#)]

166. Hönnige, J.R.; Colegrove, P.A.; Ahmad, B.; Fitzpatrick, M.E.; Ganguly, S.; Lee, T.L.; Williams, S.W. Residual stress and texture control in Ti-6Al-4V wire + arc additively manufactured intersections by stress relief and rolling. *Mater. Des.* **2018**, *150*, 193–205. [[CrossRef](#)]
167. Ning, F.; Hu, Y.; Liu, Z.; Cong, W.; Li, Y.; Wang, X. Ultrasonic Vibration-Assisted Laser Engineered Net Shaping of Inconel 718 Parts: A Feasibility Study. *Procedia Manuf.* **2017**, *10*, 771–778. [[CrossRef](#)]



© 2019 by the authors. Licensee MDPI, Basel, Switzerland. This article is an open access article distributed under the terms and conditions of the Creative Commons Attribution (CC BY) license (<http://creativecommons.org/licenses/by/4.0/>).